Supplementary information for: Magnetostratigraphy of the Mercia Mudstone Group (Devon, UK): Implications for regional relationships and chronostratigraphy in the Late Triassic of western Europe.

Mark W. Hounslow and Ramues W. Gallois

This supplementary information contains the following:

- Section S1: Additional lithological details of the members and sections, section sampling details and detailed logs of the sampling locations (Figs. S1.1 to S1.7 and Table S1.1). Inferred sequence stratigraphic boundaries (Table S1.2).
- Section S2: Magnetic mineralogy details (Figs S2.1 to S2.10)
- Section S3: Details about the low stability component, stratigraphic distribution of the blocking temperatures ranges of the LT and ChRM components (Figs S3.1 to S3.6). Demagnetisation diagrams for representative specimens (Figs. S3.7 to S3.9), mean directions and reversal tests of formation units in MMG (Table S3.1).
- Section S4: Summary of the virtual geomagnetic pole (VGP) data in relationship to other Triassic poles from stable Europe (Fig. S4.1 and Table S4.1)
- Section S5. Reference magnetostratigraphic sections and the GPTS-B for the Norian and Rhaetian (Figs. S5.1 to S5.4)
    - S5.1 The upper Chinle Group/Fm magnetostratigraphy and U-Pb dates
        - S5.1.1. Petrified Forest National Park (PEFO), Arizona (Fig. S5.3)
        - S5.1.2. Chama Basin, New Mexico
        - S5.1.3 Sangre de Cristo Mountains and Tucumcari Basins, New Mexico
        - S5.1.4. Construction of the Chinle Fm composite (Fig. S5.4)
- Supplementary references
- All the specimen-based data reported here and that from the Otter Sandstone Fm in the associated Excel file.

S1. Section sampling details and lithological logs

The lower parts of the cliffs are locally partially obscured by landslide debris (main text Fig. 1), and the uppermost parts comprise vertical cliffs composed of Cretaceous age Upper Greensand Formation and Chalk Group sediments that rest unconformably on the MMG. A

low easterly dip (2-3°) allows much of the MMG succession to be examined at or a little above beach level. The sections can only be accessed at Sidmouth, Salcombe Mouth, Weston Mouth, Branscombe Mouth and Seaton (main text Fig. 1). The sections in the highest part of the MMG, the Haven Cliff Mudstone Member and the Blue Anchor Formation, crop out east of the outfall of the River Axe at Haven Cliff to Culverhole Point. Some of the sections are inaccessible at high tide, and some are prone to relatively frequent rock falls and landslides, factors which need considering if planning visits.

The sections sampled are:

A) Sidmouth to Salcombe Mouth (sample code MS; main text Fig. 2; SI Fig. S1.1): This section is between the outfall of the River Sid and Salcombe Mouth with the sampling extended up the cliff/gully at the Salcombe Mouth end of the section (from MS40 to 43; Figs. 2; S1.2). This is essentially the section studied by Creer (1955, 1959), although our sampling probably extends beyond the 52 m examined by Creer.

B) Salcombe Mouth to Hook Ebb (sample code MD; main text Fig. 3, SI Figs. S1.2, S1.3): The youngest sample is 17.5m below the base of the DMF which was inaccessible above Hook Ebb at the time of sampling.

C) Strangman's Cove (code MW; Fig. 4, SI Figs. S1.3, S1.4): This is the type section of the DMF and was sampled by Baranyi et al. (2019) for palynology. The quality and extent of the exposure here varies from year to year, so the sampling was done over several years between 2000 and 2014, with the later sampling through the base of the DMF into the top of the Hook Ebb Mudstone, which had not been exposed in earlier years. Initial data showed many magnetozones in the DMF, so later additional sampling included many fill-ins, located onto the same logs. Above the DMF are the red mudstones of the Littlecombe Shoot Mudstone Mb (top of Fig. 4). These are partly decalcified high in the cliff at this locality, so upward sampling was limited here. This upper part overlaps with the better preserved MMG at the Littlecombe Shoot west section.

D) Littlecombe Shoot west (sample code ML; lower panels in main text Fig. 5, SI Fig. S1.4): At the base of the section, weathered/slipped DMF mudstones are overlain by red mudstones of the Littlecombe Shoot Mudstone Mb. The member contains two prominent beds of sandstone which act as laterally persistent marker bands in the cliffs.

E) Littlecombe Shoot east (sample code SH; upper panels in main text Fig. 5, Figs. S1.4, S1.5): This short section, in a steep part of the cliff, overlaps with the sandstone beds in the top part of the Littlecombe Shoot west section. Between Littlecombe Shoot west and Red Rock [SY1984 8807] the lower cliffs are obscured by extensive landslide deposits and vegetation. In the absence of evidence for faulting or change of bedding dip angle, the gap between the top of the youngest Littlecombe Shoot-east exposure and the base of the Red Rock- Branscombe Mouth section is estimated at 15 m. This is a ~22 m magnetostratigraphic sampling gap to the lowest sample in the overlying Red Rock-Branscombe Mouth section. The sampling gaps are clear in the detailed logs below.

F) Red Rock to Branscombe Mouth (code MB; main text Fig. 6, SI Fig. S1.5): Three sub-sections were sampled covering an interval from 2.5 m above the exposed base of the Red Rock Gypsum Mb to 54 m into the Seaton Mudstone Mb (SI Fig. S1.5). Strong colour banding allowed sub-sections to be correlated easily. The youngest part of the section exposes red mudstones with cm-thick sandstone laminae high in the cliff west of Branscombe Mouth, overlain unconformably by the Cretaceous Upper Greensand Formation (Fig. 6).

G) Seaton Cliffs (code SE; main text Fig. 7, SI Fig, S1.6): Samples collected in 2003 from two sections in the Seaton Mudstone Mb fall within the Axe Valley Fault Zone at Seaton. The section sampled at Seaton (SI Fig. S1.6) was the best exposed succession in a group of five fault-bounded blocks that lie within the fault-bounded valley of the River Axe. Most of the successions within these fault blocks are poorly exposed due to landslides. Seismic-reflection surveys across the valley indicate that both the Axe Valley boundary faults downthrow the top of the DMF ~100 m to the west (Edwards and Gallois 2004 fig. 6). To the west of the sampled section, up to a maximum of 40 m of Seaton Mudstone (older than the sampled section) is poorly exposed within the valley, and although some of the lithologies are like those in the Branscombe section (SI Fig. S1.5), the Red Rock Gypsum is not exposed. To the east of the sampled section, up to a maximum of 40 m of partially exposed Seaton Mudstone is lithologically different from that exposed in Haven Cliff. The regional east-directed dip of ~2° is maintained throughout these easterly sections which suggests that they are younger than the sampled section. Neither the Haven Cliff Mudstone Mb nor the BAF are exposed in the Axe valley fault system. These factors, and the fact that marker-bed correlation cannot be made between the Seaton sections and those

outcrops to the west of the town at Branscombe Mouth or east in the Haven Cliff section, suggest that the sampled Seaton section likely falls between the top and base of the sampled sections west and east of the town. Estimates of the thicknesses of the successions exposed in the individual fault blocks suggests that the sampled section represents ~25% of the total Seaton Mudstone Mb in the fault blocks. At the time of writing, these sections are now in a poorer and less accessible condition than when sampled, due to a combination of landslides and sea-defence works.

H) Haven Cliff (code HC, main text Fig. 8, SI Fig. S1.7). This covers the upper part of the Branscombe Mudstone Fm and most of the Blue Anchor Fm (BAF), although an additional ~13 m from the top of the BAF was not sampled (Fig S1.7). This section was also sampled in a second field season to refine polarity boundary positions.

1:100 scale when printed in A3 format

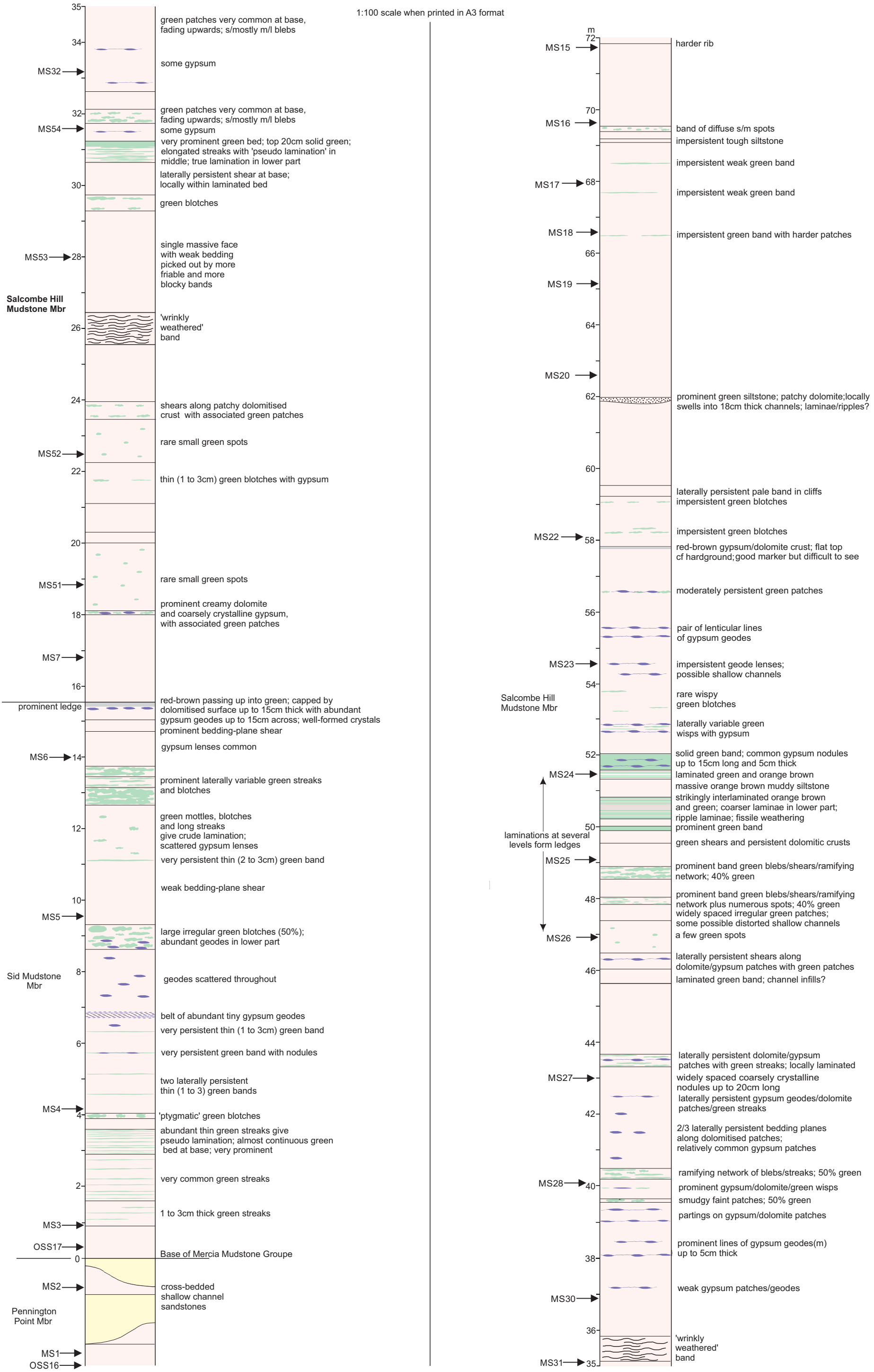

Figure S1.1. Sid outfall (Sidmouth) [SY 1290 8733] to Salcombe Mouth [SY 1462 8765]. Arrows indicate the sample number (MS). The OSS codes relate to the samples of Hounslow & Mcintosh (2003). See Fig. S1.6 for key. Not shown on this log are MS55, MS56 at 4.45 m and 9.67m respectively below the base of the MMG. MS56 is 0.23m below OSS3 measured by Hounslow & McIntosh (2003).

Figure S1.2. Salcombe Mouth [SY 1462 8765] to Hook Ebb [SY 1566 8776] section (MD samples). The MS samples belong to the Sidmouth to Salcombe Mouth section.

1:100 scale when printed in A3 format

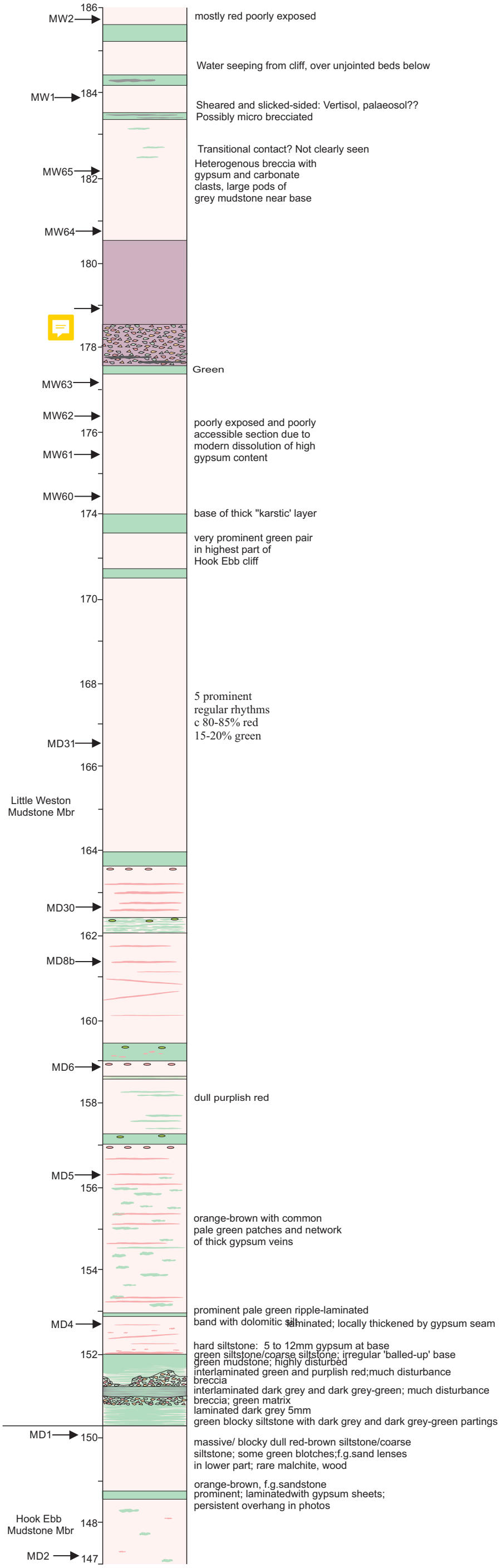

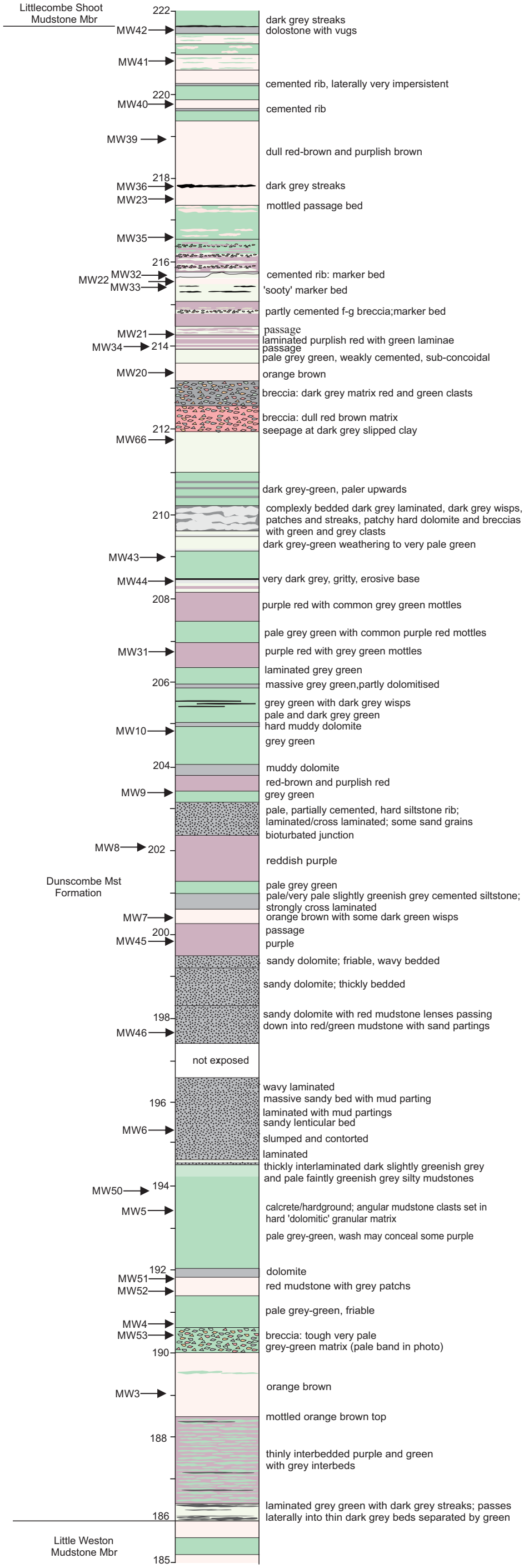

Figure S1.3. The upper part of the Salcombe Mouth -Hook Ebb section Hook Ebb [SY 1566 8776] (MD samples), and lower and mid part of the Strangeman's Cove (MW sample codes, [SY 1691 8793] section.

1:100 scale when printed in A3 format

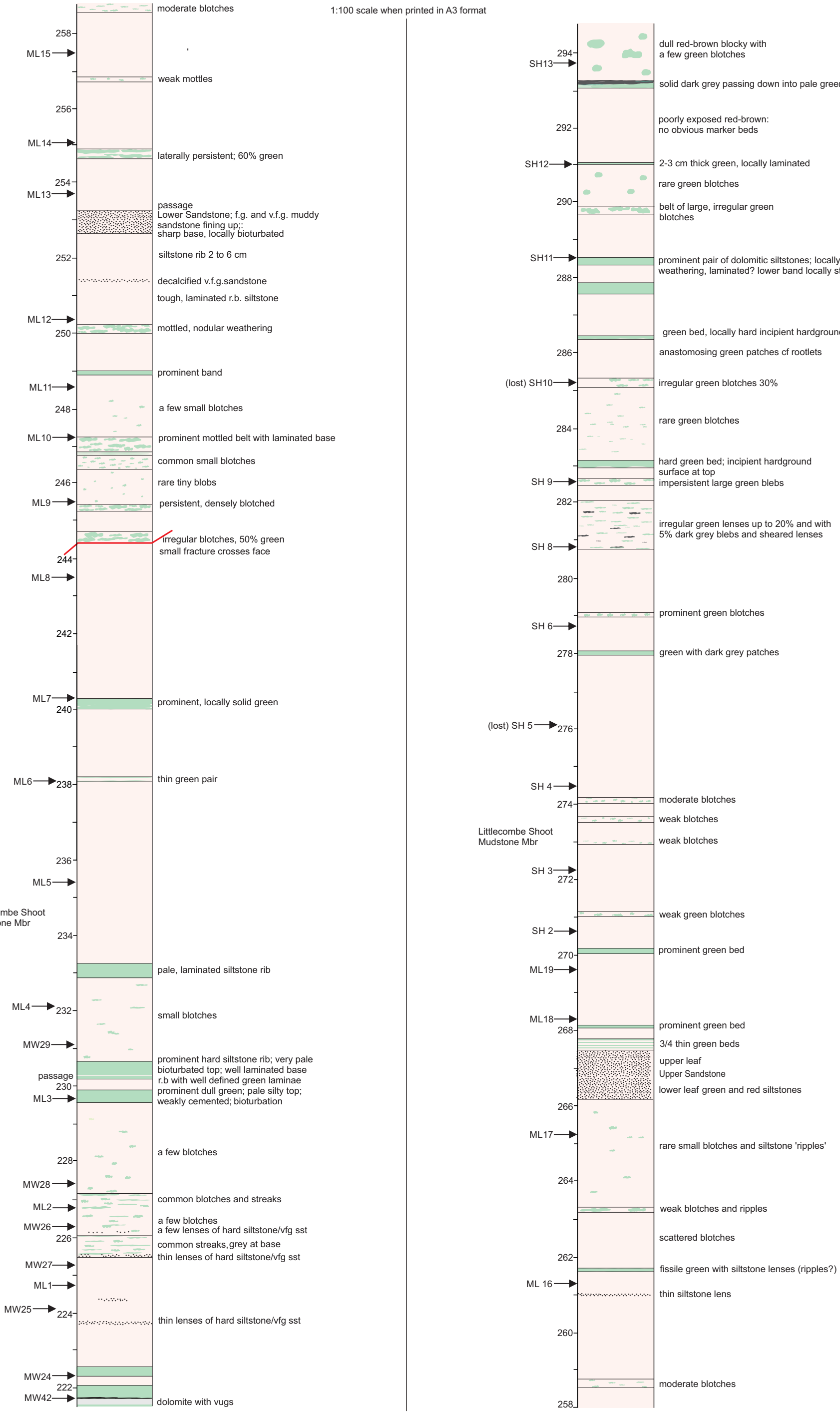

Fig. S1.4. The upper part of the Strangeman's Cove section (MW sample codes [SY 1691 8793]) and the Littlecombe Shoot sections (ML and SH sample codes) [SY 1828 8815].

1:100 scale when printed in A3 format

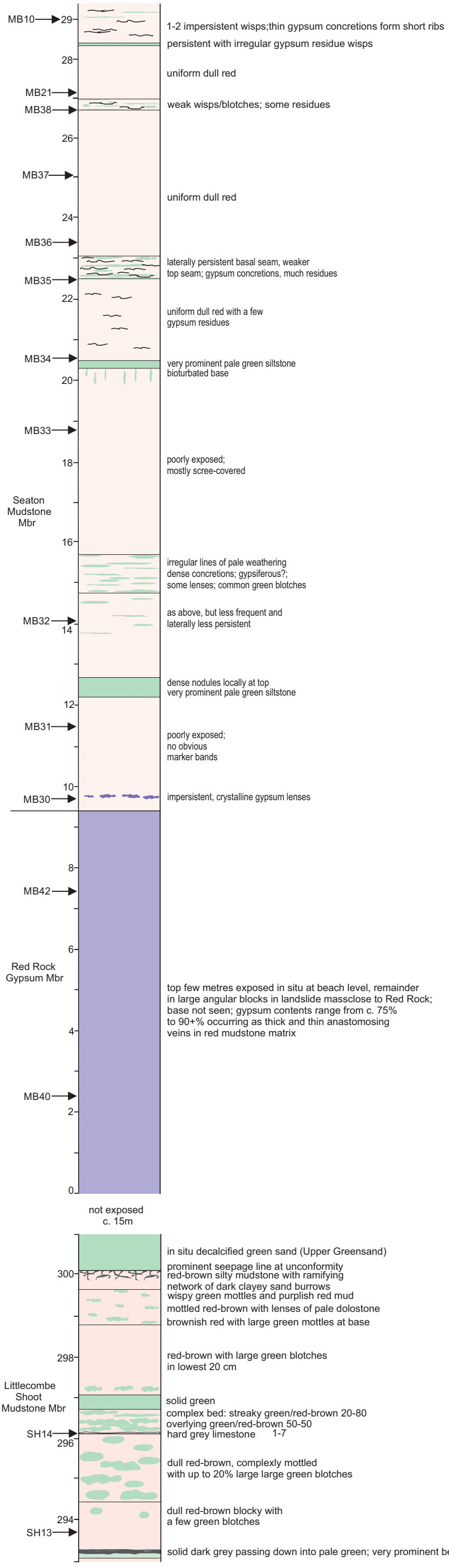

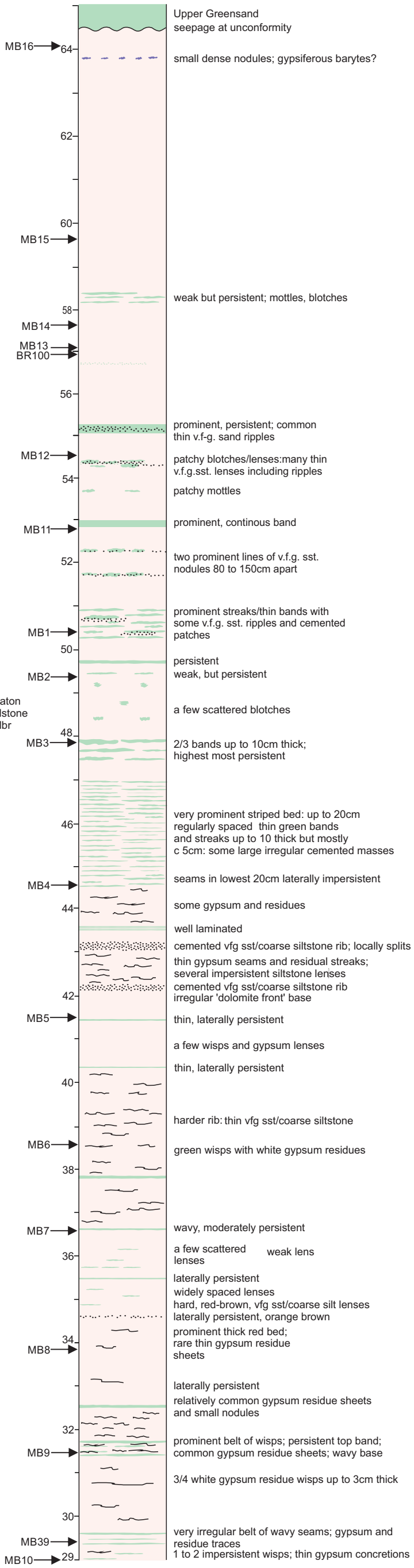

Fig. S1.5 The top-part of the Littlecombe Shoot section (SH sample codes) and the Branscombe Mouth section (MB sample codes). Red Rock [SY 1984 8807 sample MB40] to Branscombe [SY 2029 8815, sample MB16].

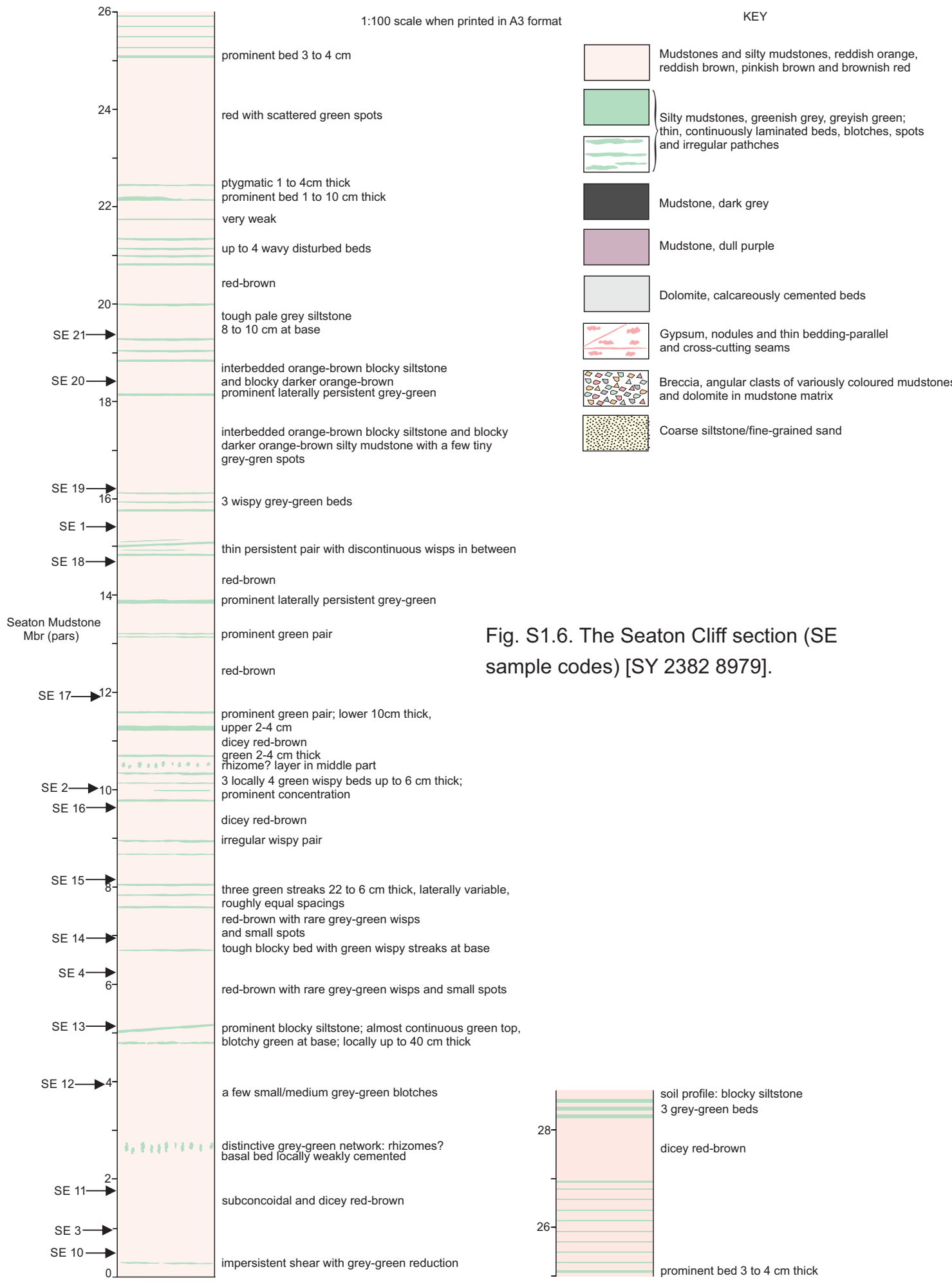

Fig. S1.6. The Seaton Cliff section (SE sample codes) [SY 2382 8979].

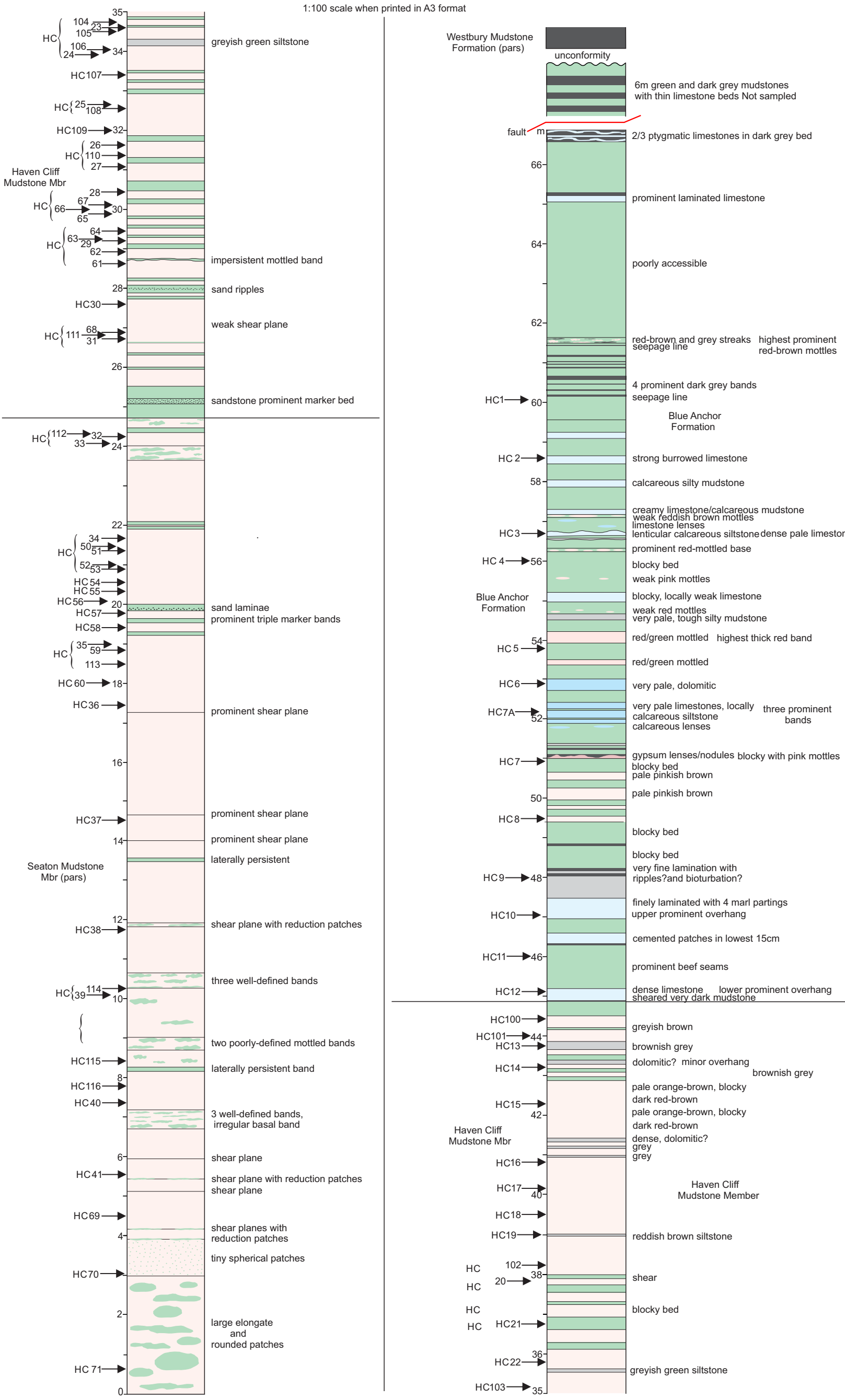

Figure S1.7. Haven Cliff [SY 2565 8972 to SY 2730 8936].

Supplementary Table S1.1. Lithology of the lithostratigraphic units of the sub-divided Mercia Mudstone Group. [1] of Sidmouth Mudstone Formation, [2] of Branscombe Mudstone Formation.

Unit name	**Lithology/ *defined location***
Blue Anchor Formation	Interbedded grey, green and rarely red calcitic and dolomitic mudstones.
[2]Haven Cliff Mudstone Mb	Interbedded green and red dolomitic and calcitic mudstones, with occasional siltstones (the 'variegated marls' of older usage).
[2]Seaton Mudstone Mb	Orange-red and occasionally green calcitic and dolomitic mudstones and occasional thin siltstones.
[2]Red Rock Gypsum Mb	Gypsum-cemented orange-red mudstone, with commonly developed mud breccia texture
[2]Littlecombe Shoot Mudstone Mb	Orange red mudstones with several prominent sandstone horizons and occasional green siltstone horizons.
Dunscombe Mudstone Fm (DMF)	Interbedded pale to dark grey, pale green, dark reddish brown to purple and orange red calcareous mudstones. Also has well-developed thin white siltstones and silty sandstones. Some mudflake conglomerates are also present. Solution breccias indicate thick former halite and gypsum deposits.
[1]Little Weston Mudstone Mb	Interbedded orange red and dark red dolomitic and calcitic mudstones, with extensive gypsum seams and veins
[1]Hook Ebb Mudstone Mb	Orange red dolomitic and calcitic mudstones, with occasional green mudstone and siltstone bands, and common horizons of gypsum seams and veins
[1]Salcombe Mouth Siltstone Mb	Orange red dolomitic and calcitic mudstones, with several thick beds of orange-red siltstone.
[1]Salcombe Hill Mudstone Mb	Orange red dolomitic and calcitic mudstones, with occasional thin green mudstone and siltstone bands, and layers of gypsum nodules.
[1]Sid Mudstone Mb	Orange red dolomitic and calcitic mudstones, with occasional thin green mudstone and siltstone bands.
Pennington Point Mb (of Otter Sandstone Fm)	Interbedded orange-red mudstones and sheet-flood, red silty sandstones. Characterised from the underlying Otter Sandstone by the absence of calcrete conglomerates and the development of large to small sandstone and mudstone filled channels.

Supplementary Table S1.2. Location and description of inferred sequence stratigraphic boundaries in the upper part of the Otter Sandstone Formation and the Mercia Mudstone Group from the Devon coast. These placements utilise principally the clastic playa model of Talbot et al. (1994) and Vollmer et al. (2008), as also shown in fig. 16.13 of Hounslow et al. (2012). The boundaries are organised base to top= oldest to youngest.

Fm/Mb location	**Type [metre level]**	**Characteristics, sources and associated samples**
Base of Haven Cliff MM	SB/ts [ca. 455, -20.1[A]]	Fig. 15. Green Marl with intervening sandstone layer- the base of which is prominent juncture between the red mudstones below and overlying increasingly frequent green and grey mudstones.
High gamma pick in middle of the Seaton MM	mfs [ca 382]	Fig. 15. This high gamma pick can be correlated across Wessex Basin (Galllois 2003; Newell 2018b), and probably corresponds to an interval of black mudstone layers in (low tide) beach-outcrops below the sampled Seaton Section (i.e. within the mid parts of the largely unseen SS11r; Fig. 14)
Mid Red Rock Gypsum Mb	mfs [ca. 316]	Fig. 15. This marker can be recognized throughout the Wessex Basin (Gallois 2003), and probably into the Worcester Basin also (Newell 2018b).
Base of Littlecombe Shoot MM	SB/ts [221.6]	Figs. 15, 16. Dolostone overlain by a thin dark grey mudstone (MW42 sample, WE205, and immediately underlying WE207, 208 of Baranyi et al. 2019).
Dunscombe Mudstone Fm	mfs [220.6]	Fig. 16. Complex of a dolostone with immediately overlying thin grey mudstone layers interbedded in red mudstone
Dunscombe Mudstone Fm	mfs [210]	Fig. 16. Dolostone with interbedded dark grey mudstones, with some brecciation (sample WE305, of Baranyi et al. 2019). Bed L of Gallois and Porter (2006).
Dunscombe Mudstone Fm	ts [208.4]	Fig. 16. Dark grey dolostone with a gritty erosive base, Bed H of Gallois and Porter (2006) (sample MW44 and WE301 of Baranyi et al. 2019).
Dunscombe Mudstone Fm	mfs [205.9]	Fig. 16. Muddy grey to green dolostone, immediately overlying green mudstone with thin grey mudstone layers (samples WE103, WE110, of Baranyi et al. 2019). Bed G of Gallois and Porter (2006).
Dunscombe Mudstone Fm	SB [194.6]	Figs. 15, 16, Down-cutting base of the Lincombe Sandstone, marked by distinct trace fossil assemblage (Porter and Gallois 2008). Base of bed C of Gallois and Porter (2006). Immediately underlying are samples WE106, WE105 of Baranyi et al. (2019).
Base of Dunscombe Mudstone Fm	mfs [186]	Fig. 16. Laminated grey green mudstone with thin dark grey mudstone layers (sample WE003 of Baranyi et al. (2019).
Little Weston MM	SB [180.5]	Fig. 16, purple mudstone with many slickensides and micro-brecciation (a palaeosol). Top is a prominent boundary between jointed mudstones above and unjointed mudstones in the underlying 3 m.
Salcombe Hill MM	mfs, [51.6]	Fig. 15. Green mudstone with gypsum nodules in top of an interval which is well laminated. Just above sample MS24.
Base Pennington Point Mb	ts, [-20.1[B]]	As placed by Newell (2018a), using the log scale in Hounslow and McIntosh(2003)- between samples OSS2 and OSS3.
Base Chiselbury Mb	SB, [-59.1[B]]	As placed by Newell (2018a), using the log scale in Hounslow and McIntosh(2003)- their sample CB6.
Base unit II of Otterton Ledge Mb	SB, [-88.2[B]]	As placed by Newell (2018a), using the log scale in Hounslow and McIntosh (2003)- between samples PB5 and PB6, base of unit C of Hounslow and McIntosh(2003) and unit II of the Otterton Ledge Mb of Newell (2018a).

Boundaries: SB= sequence boundary (mostly maximum regressive surface), ts=transgressive surface, mfs= maximum flooding surface. MM= Mudstone Member. [A]= below the base of the Blue Anchor Fm; [B]= below base of MMG. Metre level with respect to the base of the MMG (unless otherwise indicated)

S2. Magnetic mineralogy

A large proportion of the samples have rather similar K-NRM intensity relationships, with K between 150–300 x10^{-6} SI and intensity between 1–6 mA/m (Fig. S2.1). The exception are some red and non-red lithologies from the Dunscombe Mudstone Fm (DMF), Blue Anchor Fm and the Haven Cliff Mudstone Mb, which have K below 180 x10^{-6} SI and intensity in part below 1 mA/m (Fig. S2.1).

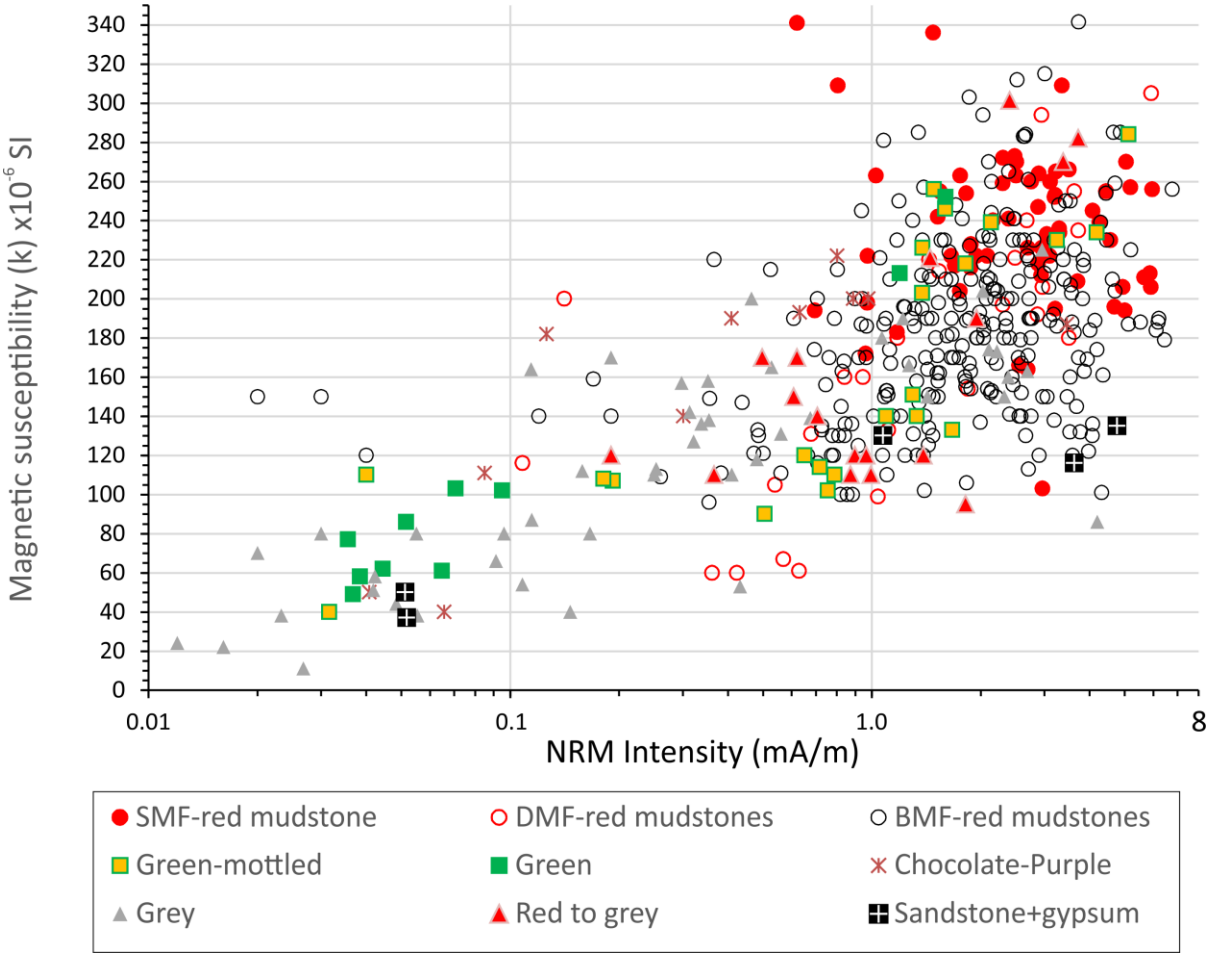

Fig. S2.1. The relationship between the NRM intensity and the magnetic susceptibility (K) for specimens. The red-mudstone samples are divided into formational groups (SMF=Sidmouth Mudstone Fm; DMF=Dunscombe Mudstone Fm; BMF=Branscombe Mudstone Fm). Other non-red samples (from both DMF, Blue Anchor Fm and Haven Cliff Mudstone Mb) are divided by dominant colour, or mixed-colour (green-mottled and red to grey). Chocolate coloured and purple-coloured mudstones are grouped together, as are sandstones (from the Lincombe Member) and gypsum (from Red Rock Gypsum Member). The major positive trend from small K and NRM intensity (predominantly grey mudstones and calcareous/dolomitic mudstones/limestones) to strongly magnetic red mudstones may be in part carbonate-content controlled, since some of those with the lowest K are also the most calcitic/dolomitic.

The natural remanence of the red mudstones is dominated by haematite which is indicated by: 1) unblocking ranges above 580ºC (Figs. S2.8, S2.9); 2) major remanence acquisition in magnetic fields above 0.1 T (Fig. S2.2a); 3) non-saturation of induced remanence (Mr) at 7 T (Fig. S2.2a); 4) magnetic extractions performed by Creer (1957) showed that the black ferromagnetic content (specularite) of the lower MMG was haematite, based on identification by X-ray diffraction. As

previously demonstrated by Creer (1961) the red mudstones of the Mercia Mudstones Group (MMG) are also rich in superparamagnetic haematite (MS5 and LP55 samples in Maher et al. 2004), which is seen in laboratory induced and remanent magnetisations (Fig. S2.2). Creer (1961) estimated that some 97% of the haematite in the MMG red mudstones should be superparamagnetic and some 0.12% of the total haematite carries the stable natural remanence.

The increase in Mr on cooling for the 2 T and 7 T remanence (France and Oldfield 2000), and the value of 56% for the % H parameter of Maher et al. (2004) indicates that sample MS5 probably contains important contributions from goethite. This is also borne out by the linear increase in Mr when cooling a 2 T or 7 T remanence acquired at 293 ºK (France and Oldfield 2000) as in Fig. S2.2c. However, SP haematite or goethite are not contributors to the ChRM which largely reside in blocking temperatures much larger than the Neel temperature of goethite (Figs. S2.8, S2.9). The absence of the Morin transition at 240 ºK in the data in Fig. S2.2c implies the bulk of the hematite is < 0.1 μm in size (Creer 1962; Maher et al. 2004). The rapid drop in J/J_{NRM} during demagnetisation at 100 -150ºC does perhaps suggest goethite may be important in carrying the LT component, or alternatively that the LT component is carried by haematite which unblocks at <350 ºC. Significantly, Maher et al. (2004) demonstrated that sample MS5 (from Sid Outfall-Salcombe Mouth section) when heated at 350ºC annealed the SP haematite which allowed emergence of the Morin transition, so demagnetisation to ca. 350ºC may simply be an annealing-induced demagnetisation, rather than true unblocking of haematite.

Non-red lithologies from the DMF and Blue Anchor Fm have a more complex mix of a soft, magnetite-like phase which fully demagnetises during AF demagnetisation (Fig. S2.9a,b,c) to a mix of haematite and this soft phase (blue curves in Figs. S2.9a,b,c), to non-red samples which are haematite dominated (Fig. S2.9d), much like the red mudstones in the DMF and other units.

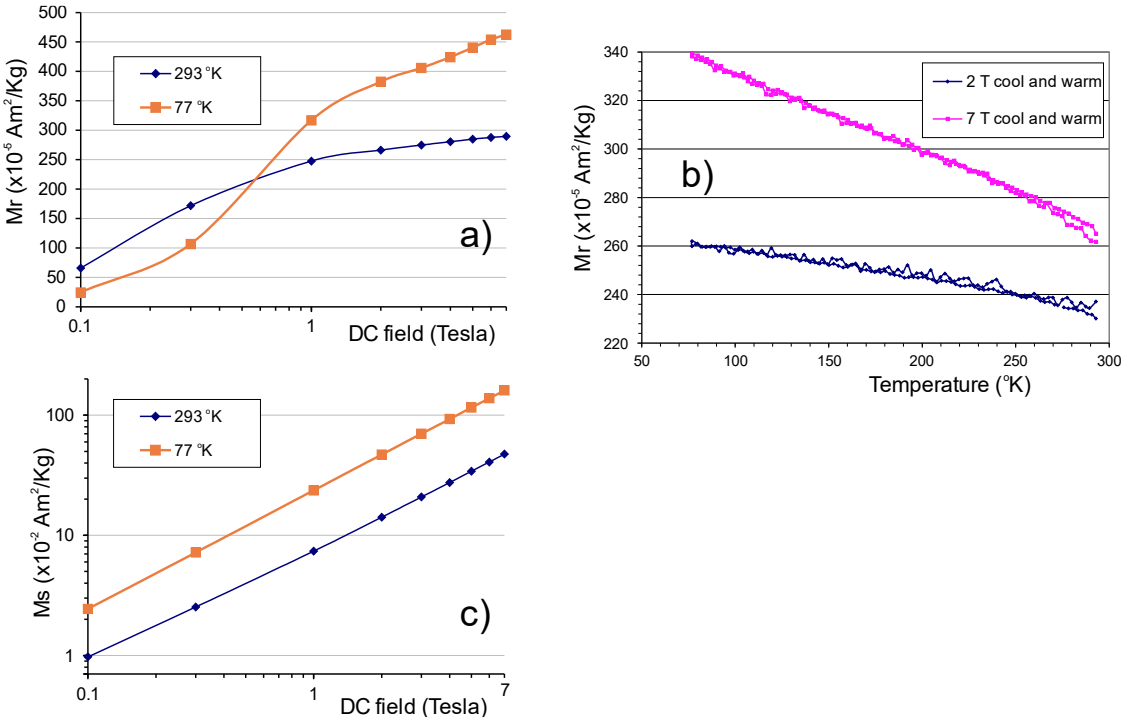

Fig. S2.2. High field and low temperature data for sample MS5 (Sid Mudstone Member). Mr= isothermal remanence, Ms=induced magnetisation. Note the non-saturation of Mr even at 7 T in a) ,

and Ms is linear with field indicating the dominance of paramagnetic/superparamagnetic susceptibility. The change in Mr between 293 and 77°K (12% at 2 T and 21% at 7 T) is smaller than the change in Ms (70% at 2T and 71% at 7 T) between 293 and 77°K indicating that most of the susceptibility is due to paramagnetic behaviour. Creer (1961, 1962) also proposed paramagnetic dominance of the susceptibility in his MMG samples from Devon and South Wales.

S2.1. Behaviour during demagnetisation

Changes in susceptibility of the red mudstones during the thermal demagnetisation heating steps tend to be small or show a gentle decline to around 400-450°C, when in many specimens there is an increase which peaks at around 500– 600°C, to be followed by the decline to 700°C (Figs. S2.3 to S2.7). Only specimens from the Seaton Section (SE code) do not show the dominance of this kind of behaviour in the red mudstones. Some red-mudstone specimens from the Hook Ebb-Strangman's Cove and Strangman's Cove-Littlecombe Shoot- Red Rock sections show more severe thermal alteration (Figs. S2.4g, h; S2.5h). Similar changes have been well documented in red-beds (Schwarz 1968; Shive and Diehl 1977, Duff 1979) and probably result either from clay mineral breakdown and/or annealing of the SP haematite fraction (remembering most of the susceptibility is due to the SP haematite fraction).

The non-red lithologies from the DMF show a range of behaviour from little change in K (Fig. S2.4d) to rather like the red-mudstone 'peaked' behaviour (Fig. S2.4c) to much larger increases in K (not well represented in the figures due to AF demagnetisation was used on these instead).

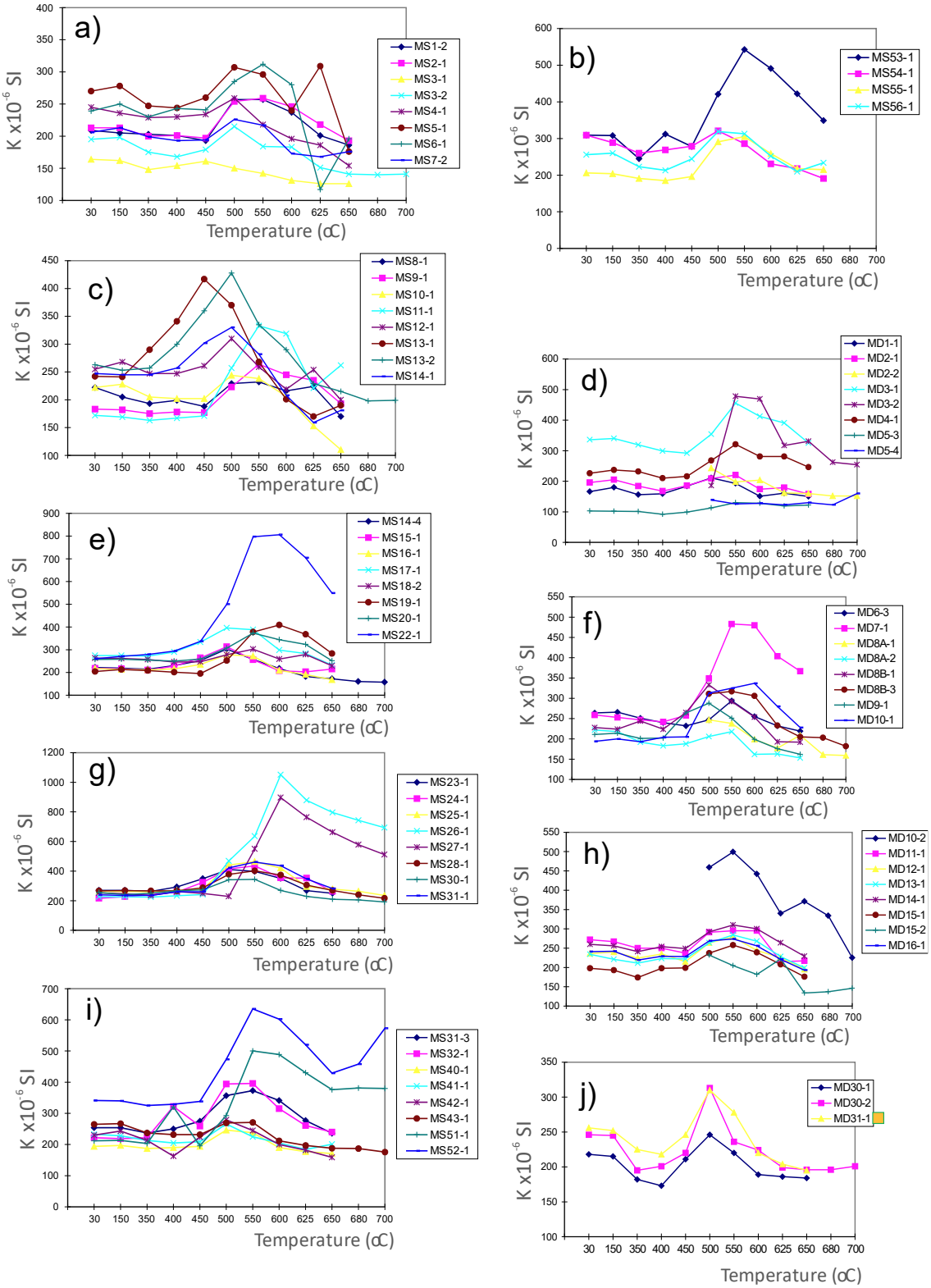

Fig. S2.3. Changes in magnetic susceptibility (K) with heating during thermal demagnetisations steps (measured at room temperature), for the Sid Outfall-Salcombe Mouth (MS) and Salcombe Mouth - Hook Ebb (MD) sections. The x-axis scale is not linear but shows the heating steps used in each case. Non red-lithologies marked with symbols as in Fig. S2.1 (e.g., MD31-1).

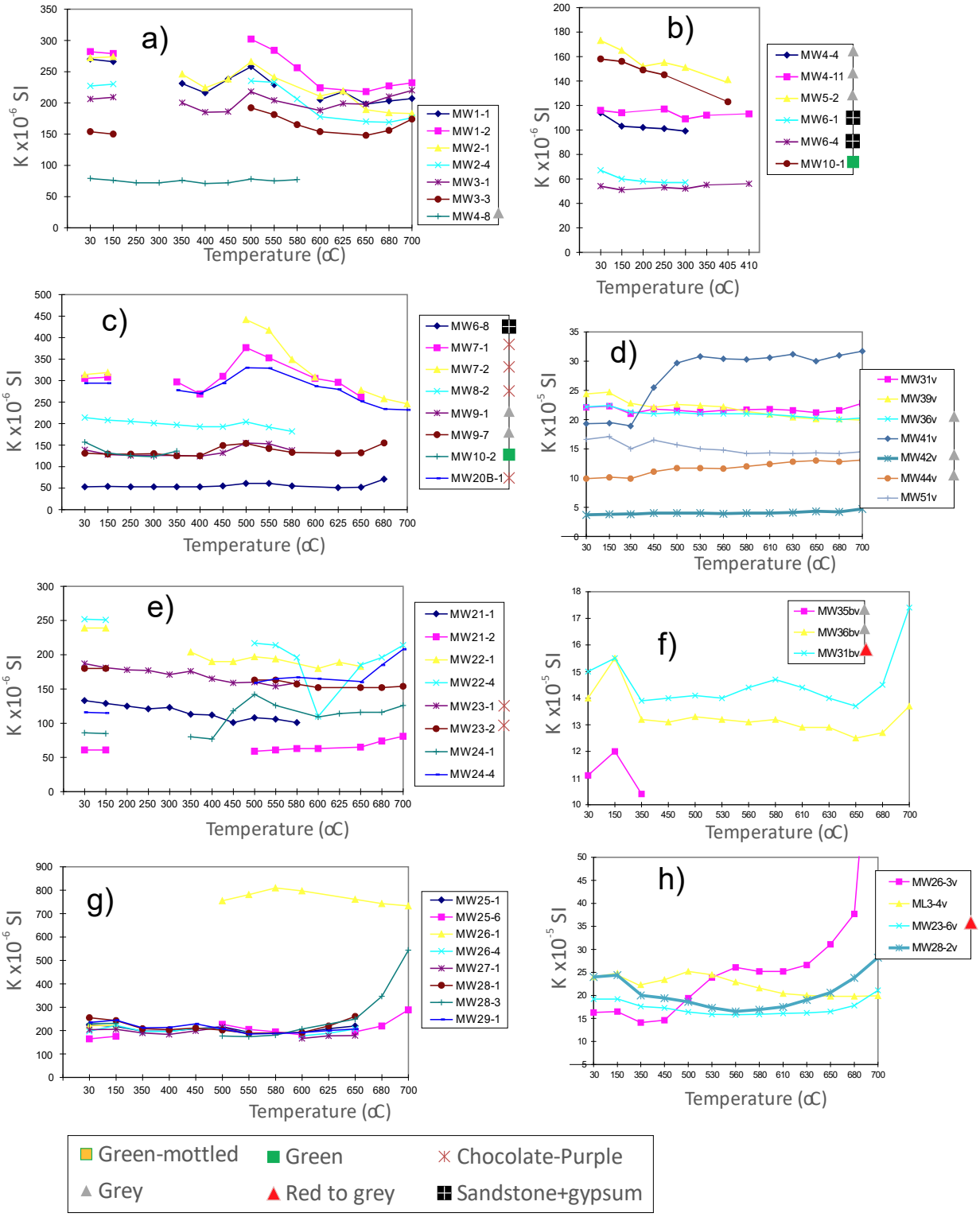

Fig. S2.4. Changes in magnetic susceptibility (K) with heating during thermal demagnetisations steps (measured at room temperature), for the Strangman's Cove (MW) section. The top-most right panel shows K for representative specimens subjected to AF demagnetisation steps. Non red-lithologies marked with symbols as in the key at the bottom (e.g., MW23-6v in h).

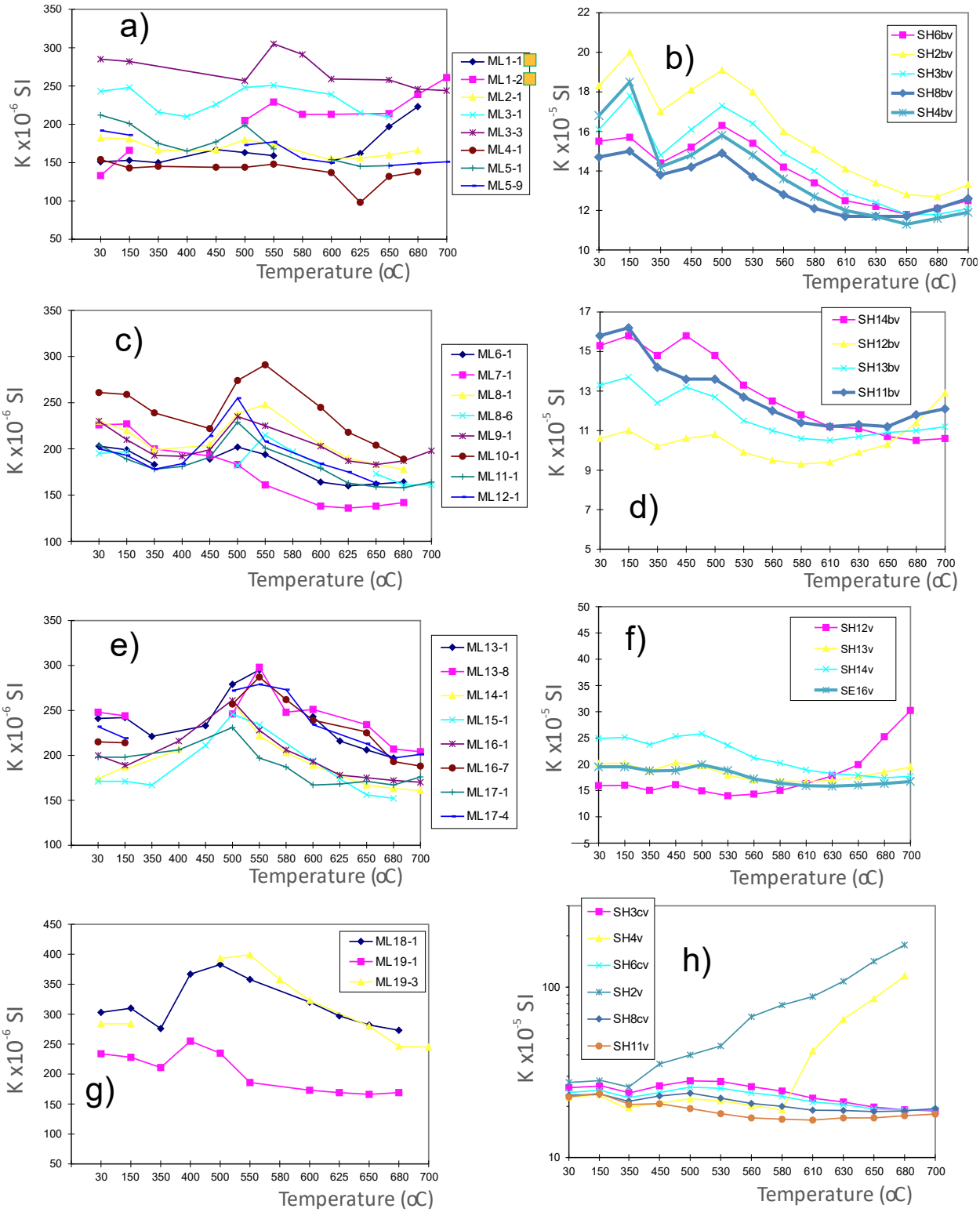

Fig. S2.5. Changes in magnetic susceptibility (K) with heating during thermal demagnetisations steps (measured at room temperature), for the Littlecombe Shoot (ML and SH) section. Note the differing scale used for K for the SH samples. Non red-lithologies marked with symbols as in the key in Fig. S2.4.

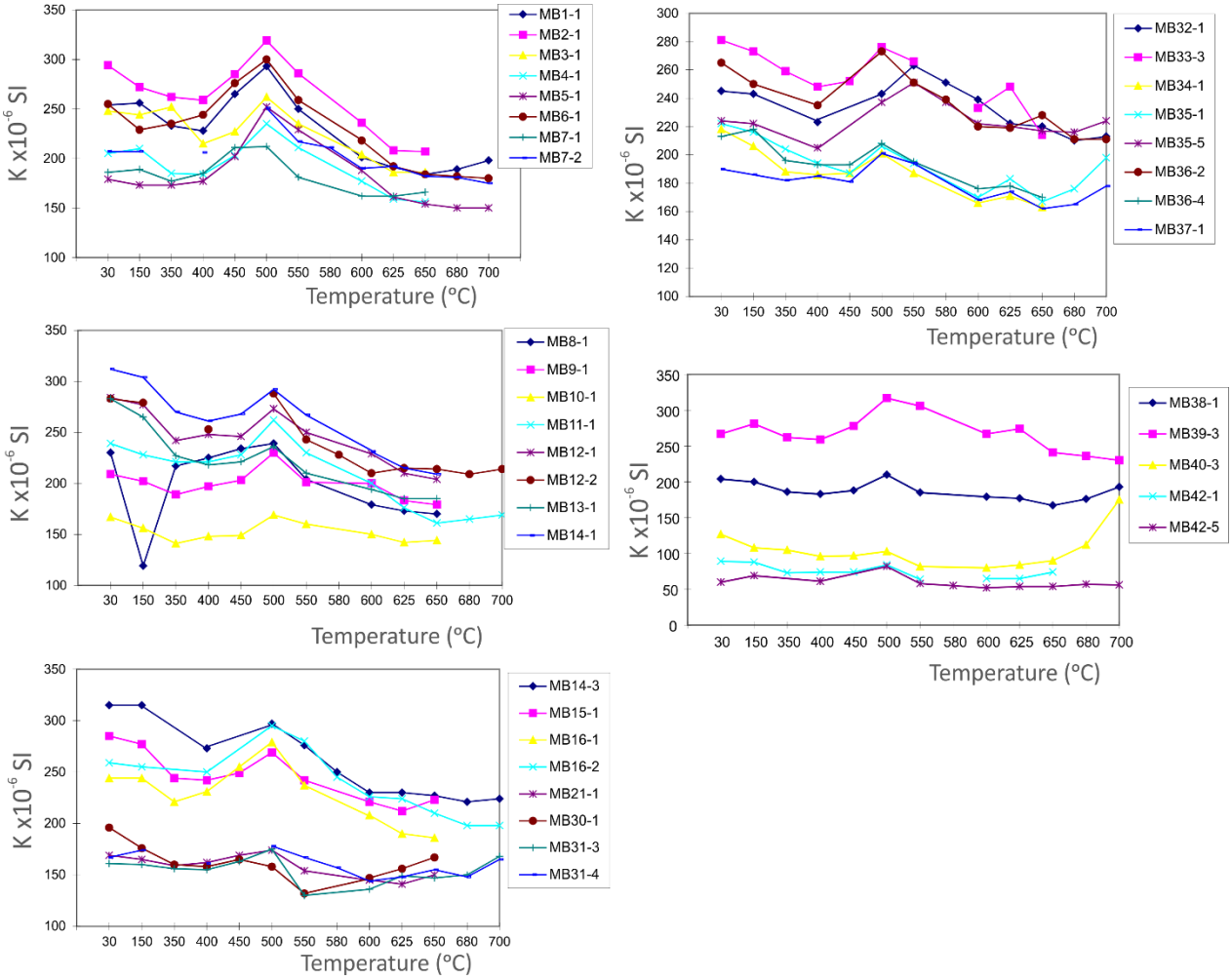

Fig. S2.6. Changes in magnetic susceptibility (K) with heating during thermal demagnetisations steps (measured at room temperature), for the Red Rock to Branscombe Mouth (MB) section.

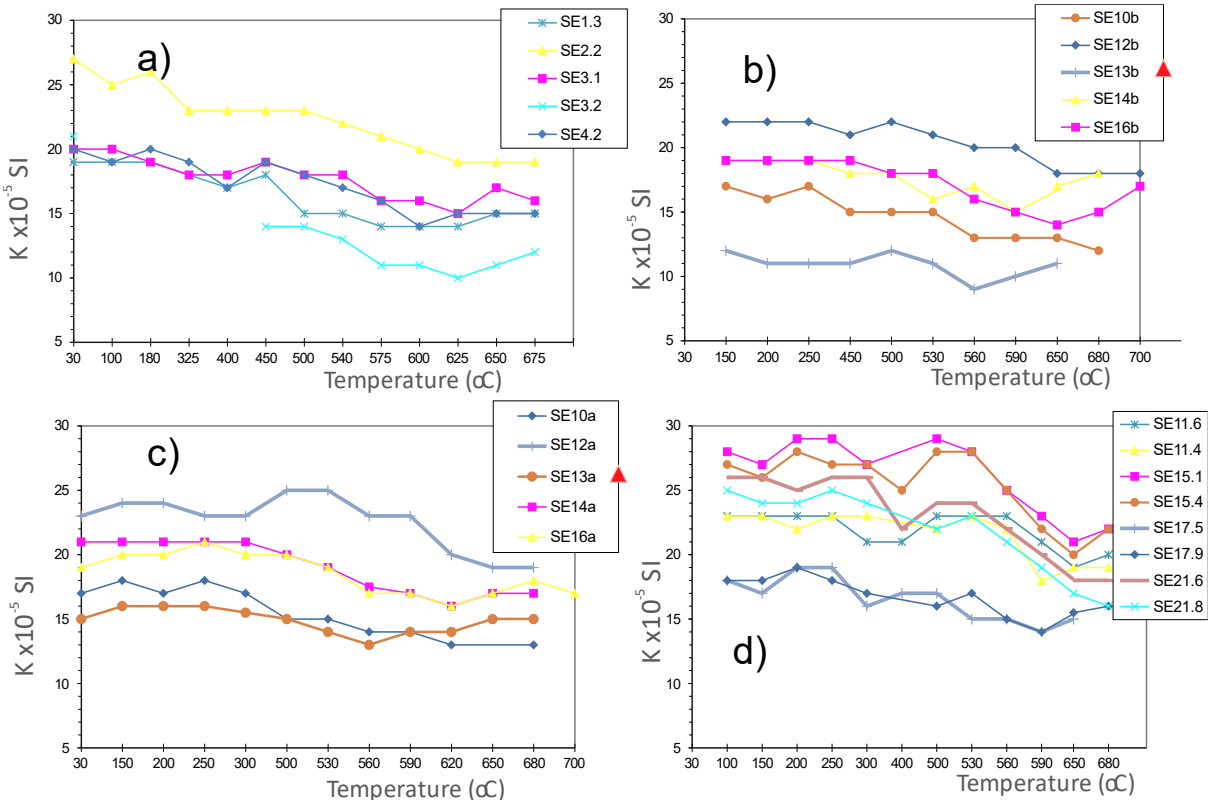

Fig. S2.7. Changes in magnetic susceptibility (K) with heating during thermal demagnetisations steps (measured at room temperature), for the Seaton Cliff section. Non red-lithologies marked with symbols using the key in Fig. S2.4.

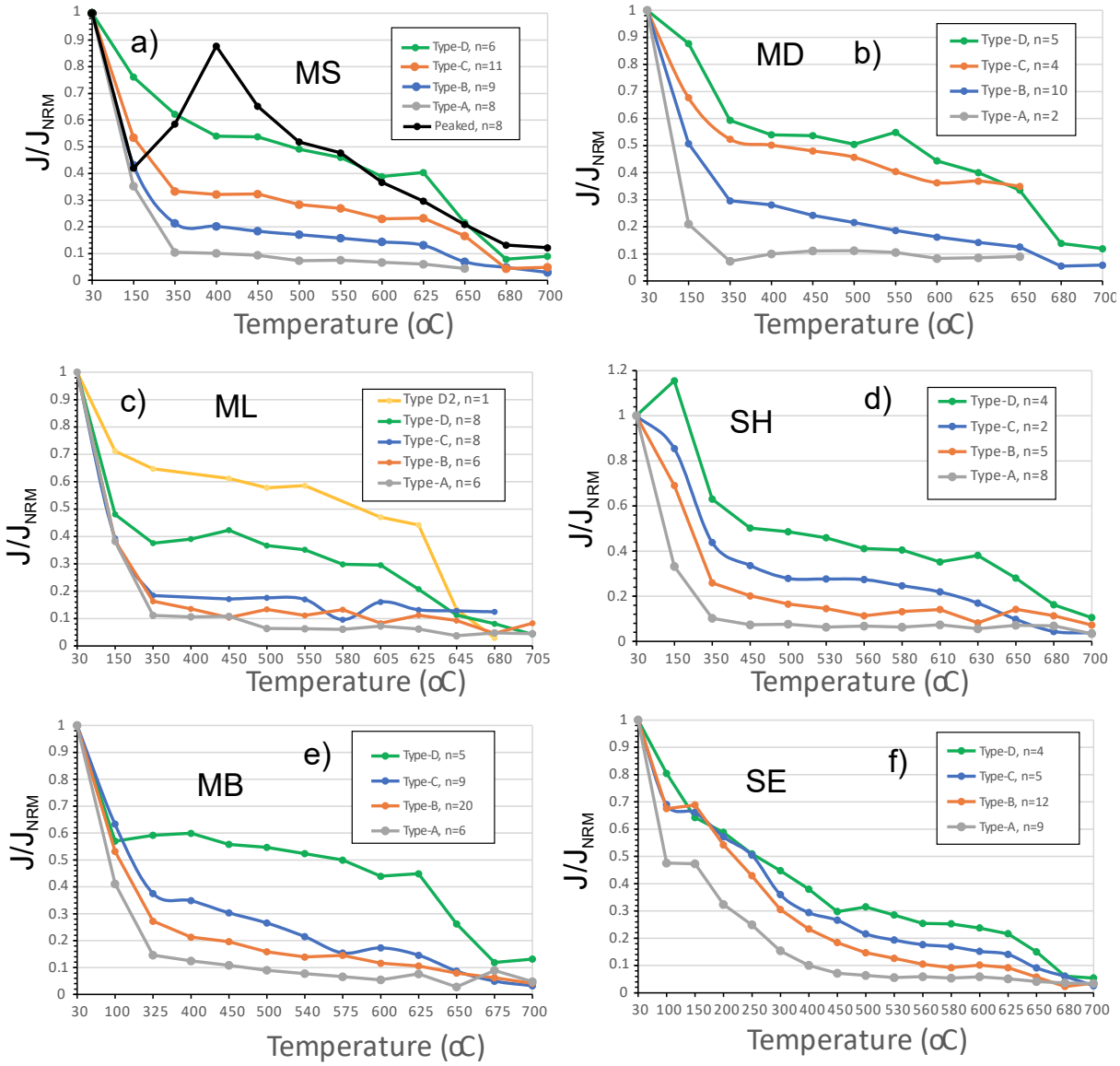

Fig. S2.8. Typical loss of normalised natural remanence (J/J_{NRM}) during demagnetisation for the red lithologies from the various sections (excluding the Strangman's Cove section shown in Fig. S2.9). In each case the curves represent an average of several sets (n= number of specimens) of similar shaped curves, divided into sets based on their J/J_{NRM} intensity between 100 and 500 ºC. These sets are divided into Types A to D (for each section) representing small retention of NRM at 100-500ºC (for Type A behaviour) to larger retention of NRM (for Type-D behaviour). The shapes of the curves are unrelated to the polarity of the specimens, as might be anticipated for remove of a normal polarity LT from reverse and normal polarity ChRM. Those from the MS section have a few specimens (both R and N ChRM) which show a peaked response at around 400ºC.

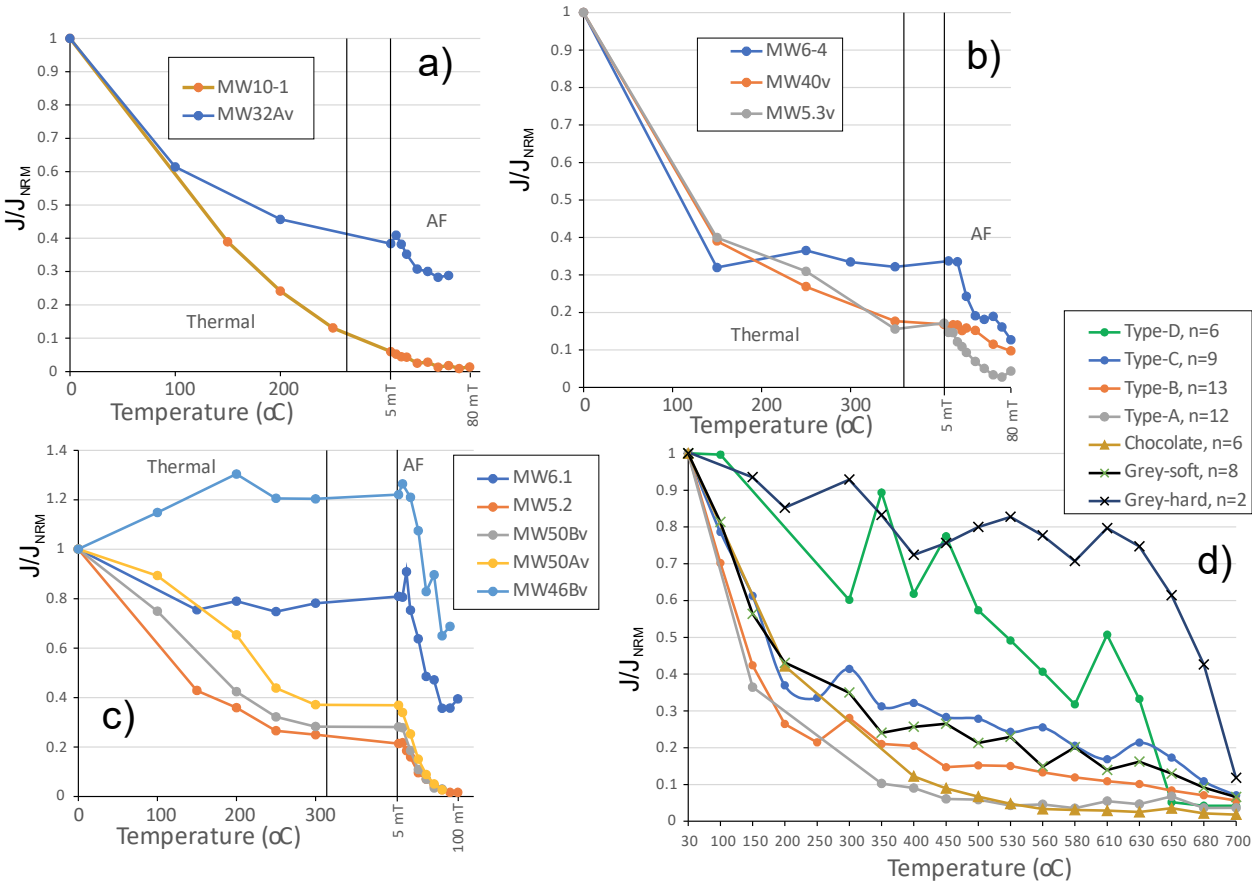

Fig. S2.9. Typical loss of normalised natural remanence (J/J_{NRM}) during demagnetisation for specimens from the Strangman's Cove section (MW code). A), B), C) show representative specimens (labelled with name) subjected to combined thermal and AF demagnetisation. Vertical lines separate the thermal and AF demagnetised steps. D) Those subjected to thermal demagnetisation alone. See Fig. S2.8 for details for red-coloured specimens (Type A to D) in D). In D) those specimens which were not red but grey or pale-chocolate coloured lithologies are also indicated. Grey lithologies either have 'soft' behaviour like the bulk of the red mudstones, or 'hard' behaviour.

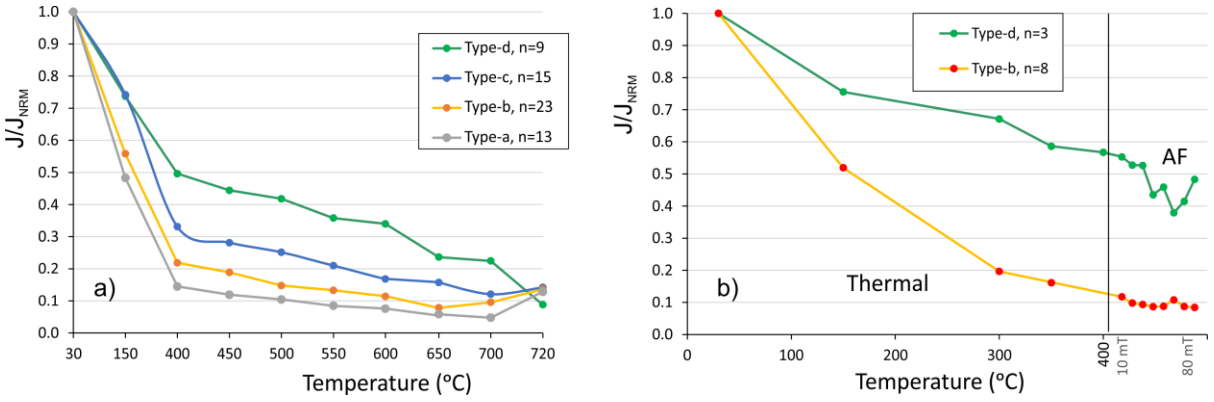

Fig. S2.10. Typical loss of normalised natural remanence (J/J_{NRM}) during demagnetisation for specimens from the Haven Cliff section (HC code). A) Curves representing an average of several sets (n= number of specimens) of similar shaped curves, divided into sets based on their J/J_{NRM} intensity between 100 and 500 °C. Type-a and Type-b in a) tend to come from the lower part of the section (lower than 13 m below the base of the BAF), and types d and c from above this -13 m level. Intensity decay is much like other samples from the MMG (Figs. S2.8, S2.9). b) Representative average J/J_{NRM} of specimens subjected to combined thermal and AF demagnetisation (all non-red lithologies).

Vertical line separates the thermal and AF demagnetised datasets. Most of the specimens in b) are from the Blue Anchor Fm, with some from the topmost the Haven Cliff Mudstone Mb. Tumbling AF demagnetisation has a minor effect in changing intensity, but a bigger effect in changing the directional data.

S3. Low temperature (LT) component, unblocking ranges of components, demagnetisation diagrams and mean directions.

The LT component is fairly scattered and shows the best grouped behaviour for the SH, ML and MW sections, with least coherence in the MS, MD, HC sections (Fig. S3.1). As Creer (1957, 1959) demonstrated the lower MMG rocks can acquire substantial short-term viscous magnetisations, as well as longer term magnetisations, likely acquired during the Brunhes. Hence, a short-term viscous component has probably contributed to some of the evident scatter in the LT component. Nevertheless, the overall grouping near the present-day geomagnetic field (Fig. S3.1e) confirms the conclusions of Creer (1957) for this low stability component throughout the MMG. The LT component dominates the total NRM magnetisation in many samples accounting for around 50% to 90% of the starting NRM (Figs. S2.8, S2.9, S2.10), typically ranging up to around the ca. 350-400 ^{o}C demagnetisation steps (Fig. S3.3a,c, S3.4a, S3.5a,c,e,g).

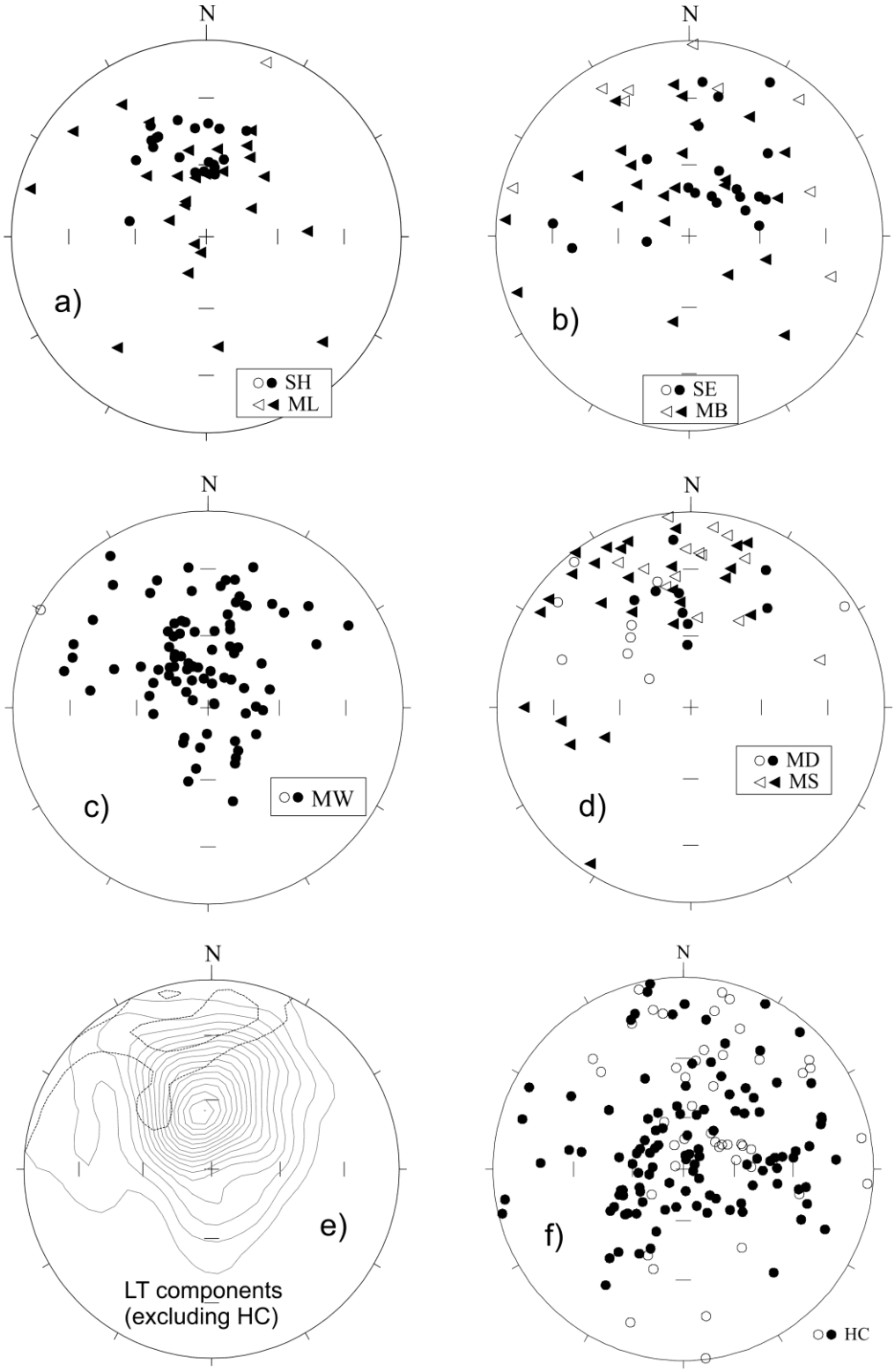

Fig. S3.1. The directional information from the low temperature component (LT) divided into divisions based on the sections (a) to d); all in geographic coordinates). See Table 2 in main text for sample codes indicating sections. e) The LT component directions contoured on the lower (solid contours) and upper hemisphere (dotted contoured), using the Kamb method and inverse area squared smoothing (binomial sigma value=3, grid size=30, contour interval=2; Vollmer 1995).

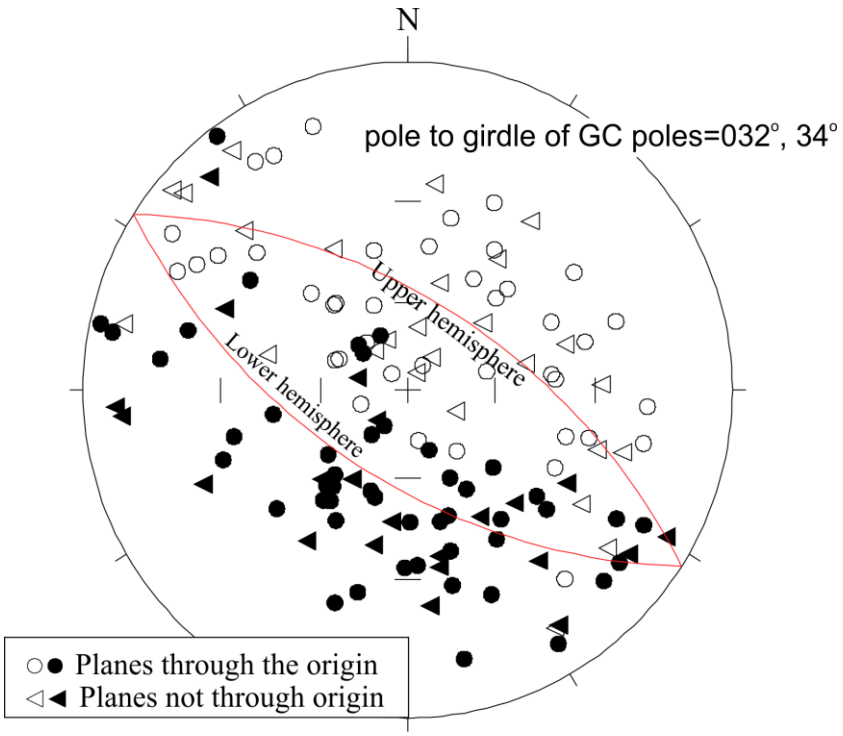

Fig. S3.2. The poles to fitted great circle (GC) planes of the ChRM directions for all the T-class specimens (in stratigraphic coordinates). The great circle shown is that orthogonal to the Fisher mean direction of all of the MMG specimens with S-class directions. Shown is the pole to the girdle defined by the GC poles (T-class specimens only), which is near to the mean direction based on the s-class specimens (main text Table 3).

The line-fit ChRM component shows a range of unblocking temperatures typically at 500ºC and above, but sometimes below this (Figs. S3.3b,d; S3.4b; S3.5b,d,f,h, S3.6b).

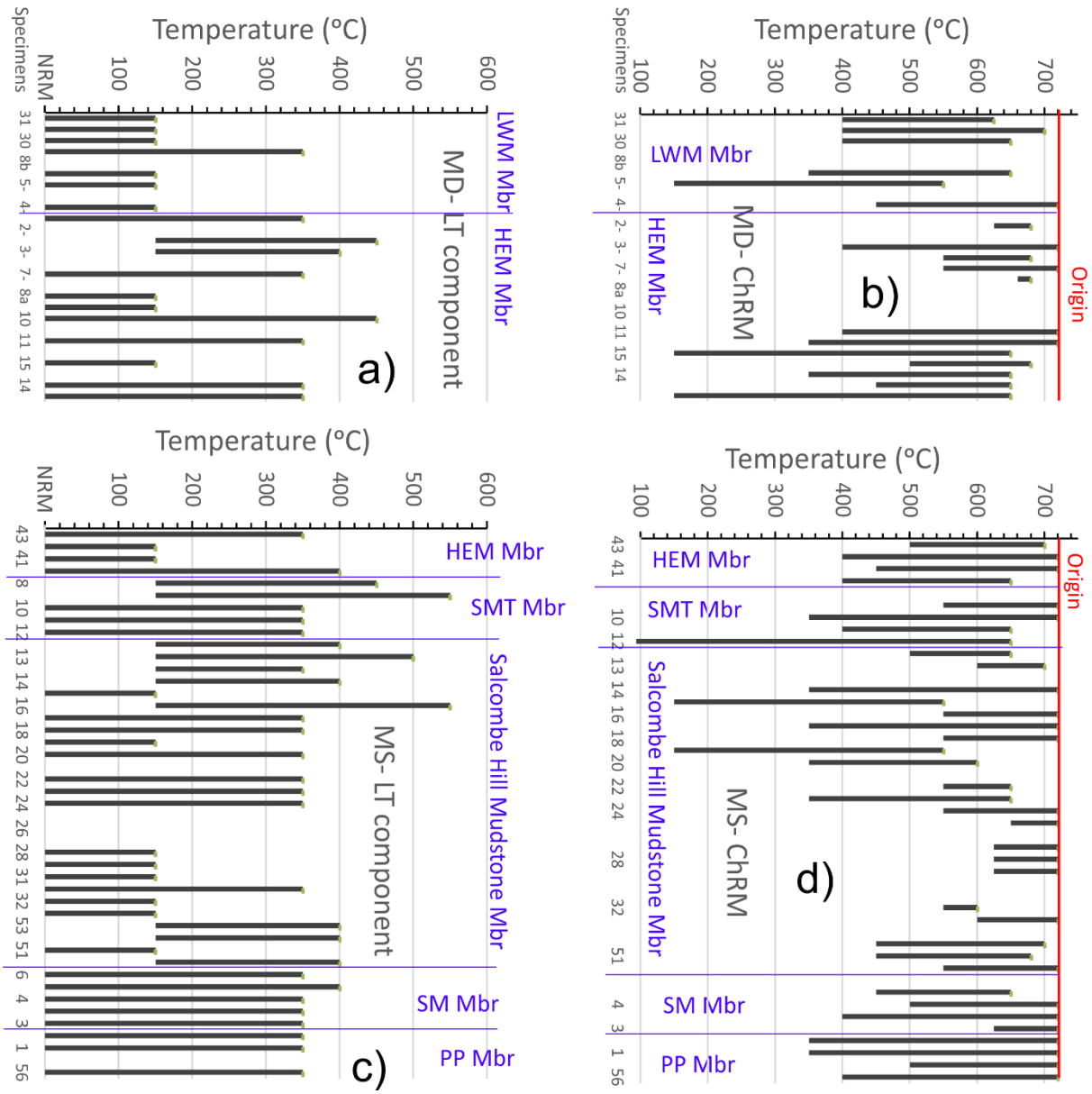

Fig. S3.3. The temperature ranges of the LT components (a and c) and the ChRM components (b and d) for samples from the Sid Outfall to Salcombe Mouth section (MS codes, c) and d)) and Salcombe Mouth to Hook Ebb (MD, a), b) section. The Y-axis shows specimens (only some sample number shown) in stratigraphic order from base to top of the section in each case. The member boundaries (in blue) are shown at the appropriate sample position. In b) and d) intersection of the range with the red vertical line indicates the ChRM component includes the vector origin in the principal component analysis. PP= Pennington Point, SM=Sid Mudstone Mb, SMT= Salcombe Mouth Mudstone Mb, HEM= Hook Ebb Mudstone Mb. LWM= Little Weston Mudstone Mb. See Figs. S1.1 to S1.7 for sample location positions on the section logs.

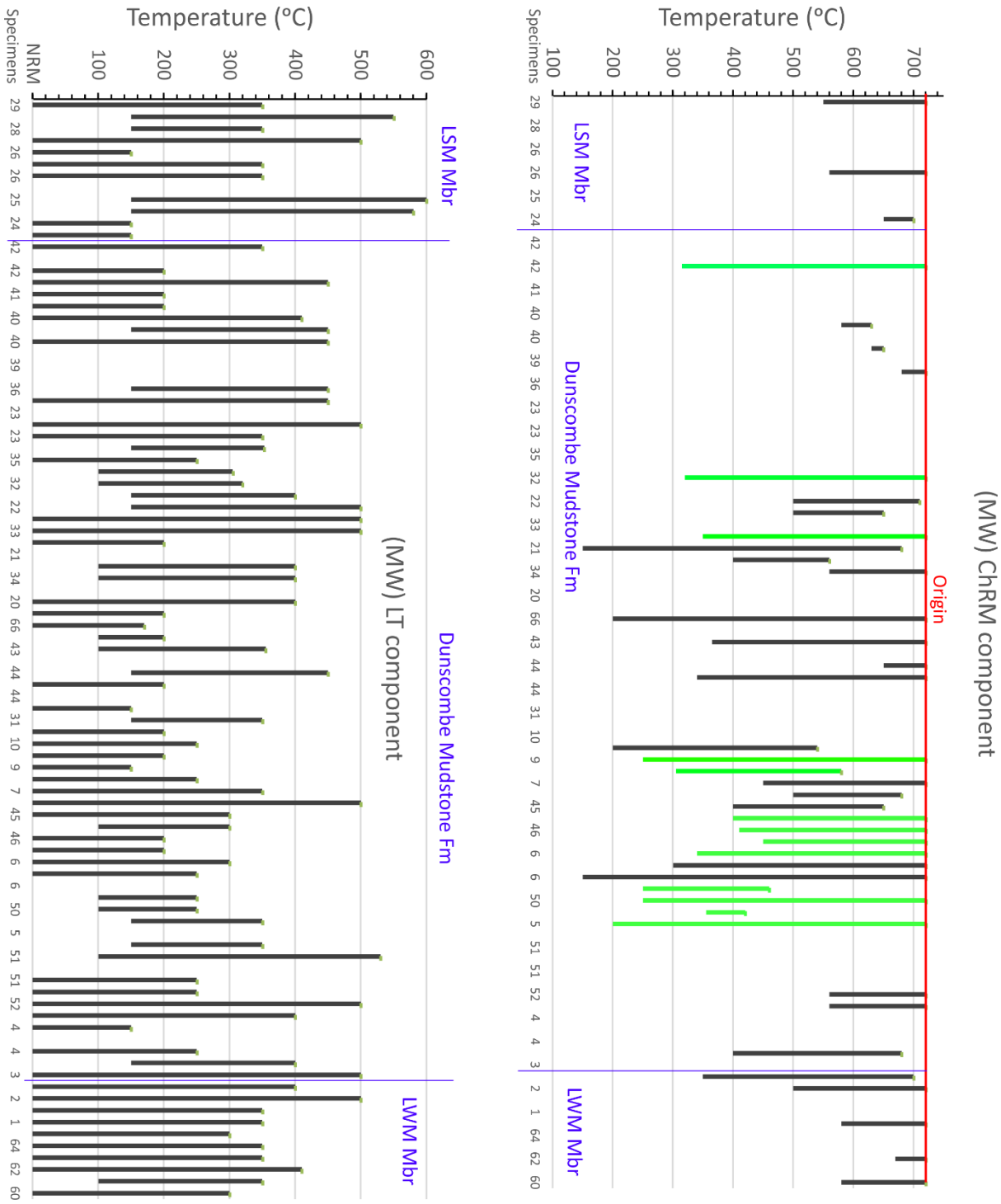

Fig. S3.4. The temperature ranges of the LT components (left) and the ChRM components (right) for the Hook Ebb-Strangman's Cove section (MW). LSM=Littlecombe Shoot Mudstone Mb. The green ranges are those which include AF demagnetisation steps, following initial thermal demagnetisation (to between 200-400 ºC). See Fig. S3.3 for other details.

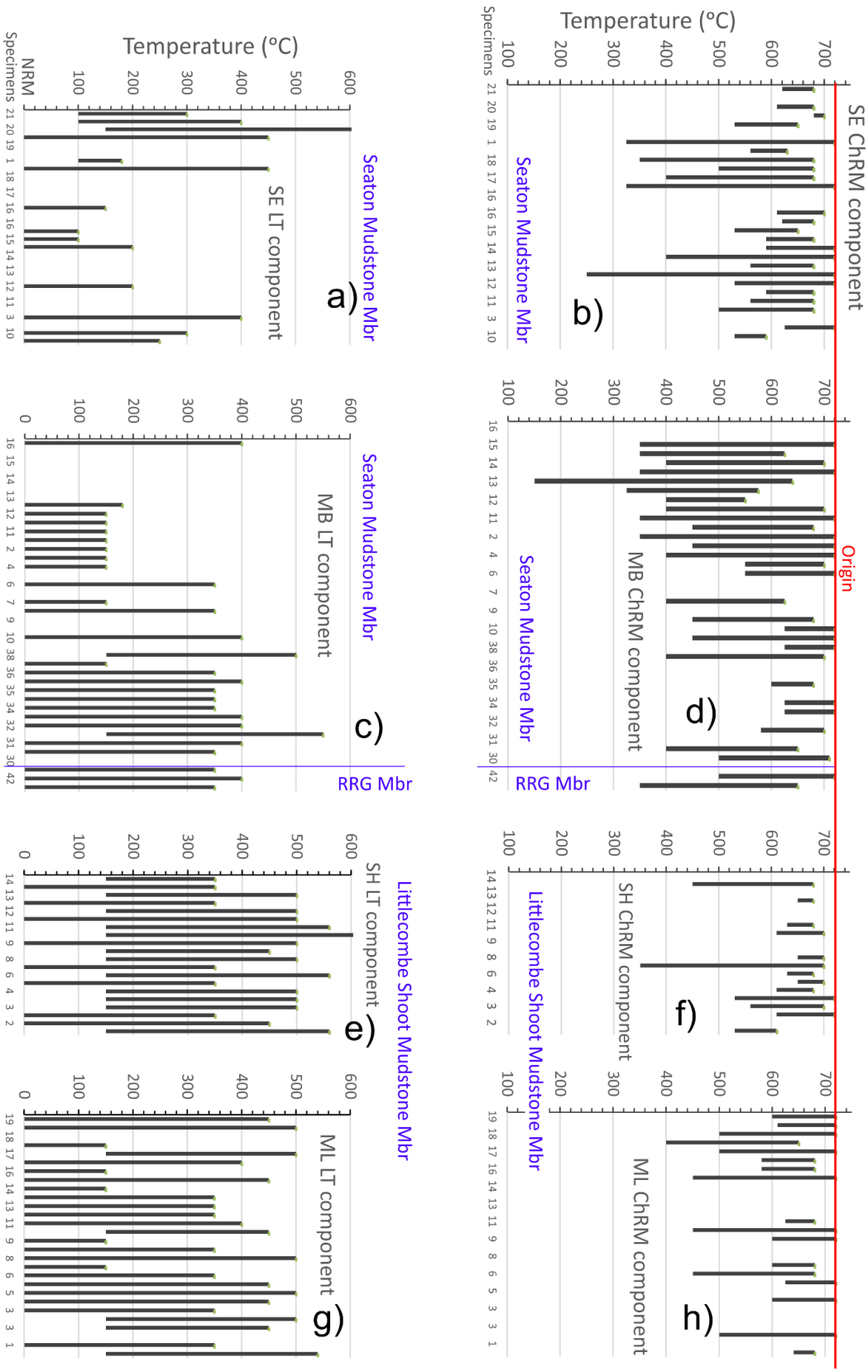

Fig. S3.5. The temperature ranges of the LT components (a, c, e, g) and the ChRM components (b, d, f, h) for the Littlecombe Shoot west section (ML), Littlecombe Shoot east (SH), Red Rock-Branscombe Mouth section (MB) and Seaton Cliffs (SE) sections. RRG= Red Rock Gypsum Mb. See Fig. S3.3 for other details.

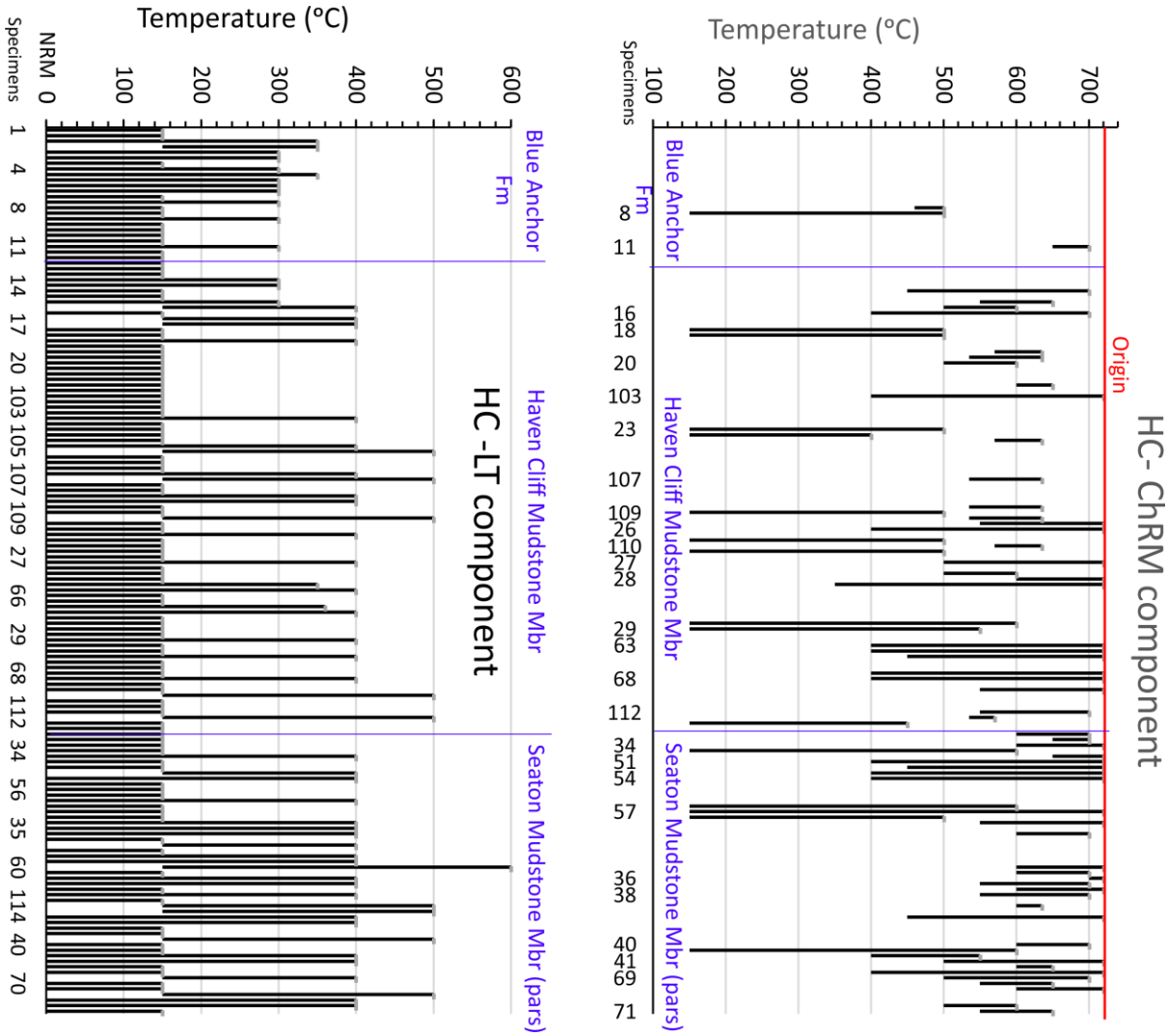

Fig. S3.6. The temperature ranges of the LT components (a) and the ChRM components (b) for the Haven Cliff section (HC). See Fig. S3.3 for other details.

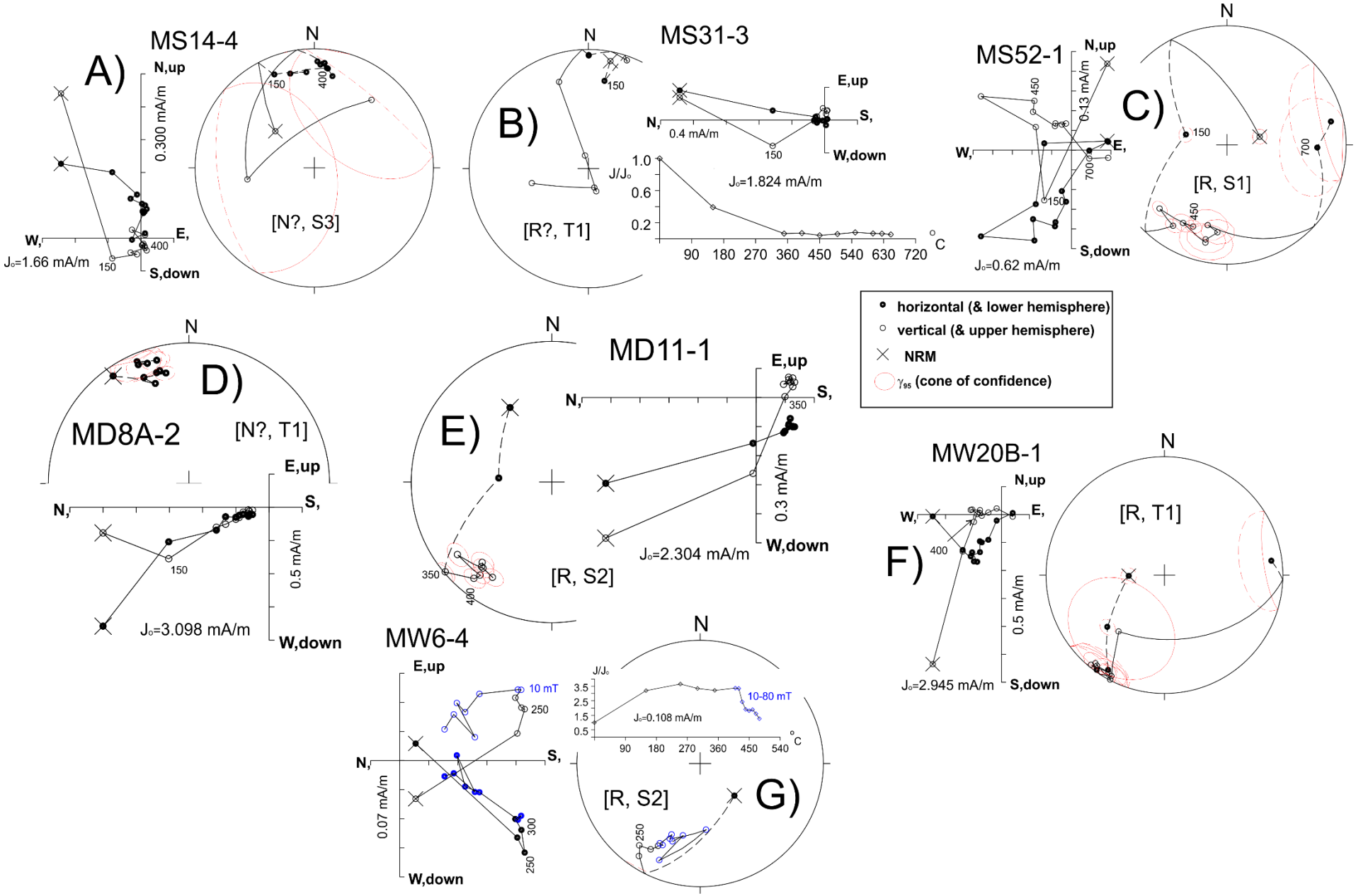
A)
MS14-4
N,up
0.300 mA/m
W,
E,
S,down
J₀=1.66 mA/m
150
400
N
[N?, S3]
B)
MS31-3
[R?, T1]
E,up
N,
S,
W,down
0.4 mA/m
J/J₀
1.0
0.6
0.2
J₀=1.824 mA/m
90 180 270 360 450 540 630 720
°C
MS52-1
N,up
0.13 mA/m
W,
E,
S,down
J₀=0.62 mA/m
450
700
C)
[R, S1]
horizontal (& lower hemisphere)
vertical (& upper hemisphere)
NRM
γ95 (cone of confidence)
D)
MD8A-2
[N?, T1]
E,up
N,
S,
W,down
0.5 mA/m
J₀=3.098 mA/m
E)
MD11-1
E,up
N,
S,
W,down
0.3 mA/m
J₀=2.304 mA/m
350
400
[R, S2]
MW20B-1
N,up
W,
E,
S,down
0.5 mA/m
J₀=2.945 mA/m
400
F)
[R, T1]
MW6-4
E,up
N,
S,
W,down
0.07 mA/m
10 mT
250
300
J/J₀
3.5
2.5
1.5
0.5
J₀=0.108 mA/m
10-80 mT
90 180 270 360 450 540
°C
[R, S2]
G)

Fig. S3.7 (previous page). Representative demagnetisation plots for the Sidmouth Mudstone and Dunscombe Mudstone formations. Showing Zijderveld plot (scale indicates that between each tick in mA/m) and stereonets of directions. Some have demagnetisation intensity (J/J_0- temperature, ^oC) plots. J_0= initial undemagnetised NRM. Stereonets display the cone of confidence values ($\gamma 95$) of Briden & Arthur (1981) from the repeat measurements (if > 5^o) of each step (some of these have been removed in some plots for greater clarity). Points marked in blue are AF demagnetisation steps, all others are thermal demagnetisation steps. Selected steps are labelled corresponding to the boundaries between the inferred extracted components and great circle planes. The inferred polarity classification and demagnetisation behaviour is indicated in the [..] brackets. Most of these are red mudstone samples, but other lithologies are indicated in the descriptions. All directional plots are in stratigraphic coordinates. Fitted components and great circle directions indicated in {..}, with LT components in geographic coordinates and others in stratigraphic coordinates (plane directions are poles to the GC plane). The third value of the ChRM or pole values in {..} is the VGP latitude value VGP_R. Heights relate to position in the subsections (shown in figures in main text).

A) MS14.4 (73.23m), normal polarity (N?) LT-component is 150-400^{o}C {318°, 9°} and ChRM is 400^{o}C-origin {000°, 21°, 60°}. B) MS31-3 (35.11 m), reverse polarity (R?) with LT component 150-400^{o}C {012°, -11°} and a plane fitted between the NRM and origin defining the magnetisation direction {281°, 04°, -73°}, shown by the trend southwards in the last four steps. C) MS52.1 (22.48 m), reverse polarity (R), with LT component NRM-150^{o}C {033°, 43°} and well-defined ChRM component 450-700^{o}C {217°, -24°, -84°}. D) MD8A-2 (36.78 m), normal polarity (N?), with LT component NRM-150°C {308°,-14°}, and a plane fitted between the NRM and origin defining the magnetisation direction {044°, -47°, 81°}. E) MD11-1 (20.66 m) with LT component NRM-350°C {343°, 38°} and ChRM component 400^{o}C to origin {221°, -17°, -78°}. F) MW20B-1, chocolate brown to dark red mudstone (27.32 m), with LT component NRM-400°C {316°, 67°}, and a plane fitted between the NRM and origin defining the magnetisation direction {303°, -8°, -86°}. G) MW6-4, white very fine-grained sandstone (9.28 m) with LT component NRM-250^{o}C {045°, 28°} and ChRM defined by the steps from 300^{o}C to the origin, including the AF steps from 10 to 80 mT {210°, -42°, -85°}.

Fig S3.8 (following page). Representative demagnetisation plots for the Dunscombe Mudstone Fm and Littlecombe Shoot Mudstone Mbr. See preamble to Fig.S3.7 for plot and labelling details.

A) MW26-3v (40.4 m), normal polarity (N) with LT component NRM-350°C {016°, 41°}, and ChRM component 560°C to origin {003°, 32°, 62°}. B) MW65_2d (3.87 m below base DMF), normal polarity (N??) with LT component NRM-300°C {099°, 74°}and ChRM component 580°C to origin {067°, 35°, 58°}. The intermediate is a composite negative inclination component in the NW. C) ML19-1 (47.39 m), normal polarity (N), with a LT component NRM -450°C {349°, 65°}, and a weak ChRM component 600°C to origin {064°, 13°, 59°}. D) ML18-1 (26.08m), reverse polarity (R) with a ChRM component 500°C to origin {207°,-19°,-82°}. E) ML2-1 (5.09 m), reverse polarity (R) with LT component NRM-150°C {23°, 41°} and ChRM component 500°C to origin (last two steps large $\gamma 95$) {202°, -31°, -79°}. F) SH6bv (11.16 m), reverse polarity with LT component 150-560°C {329°, 46°}, and ChRM component 630-680°C {224°, -25°, -79°}. G) SH11bv (20.83 m), normal polarity with LT component 150-560°C {002°, 59°}and ChRM component 630-680°C {039°, 19°, 82°}.

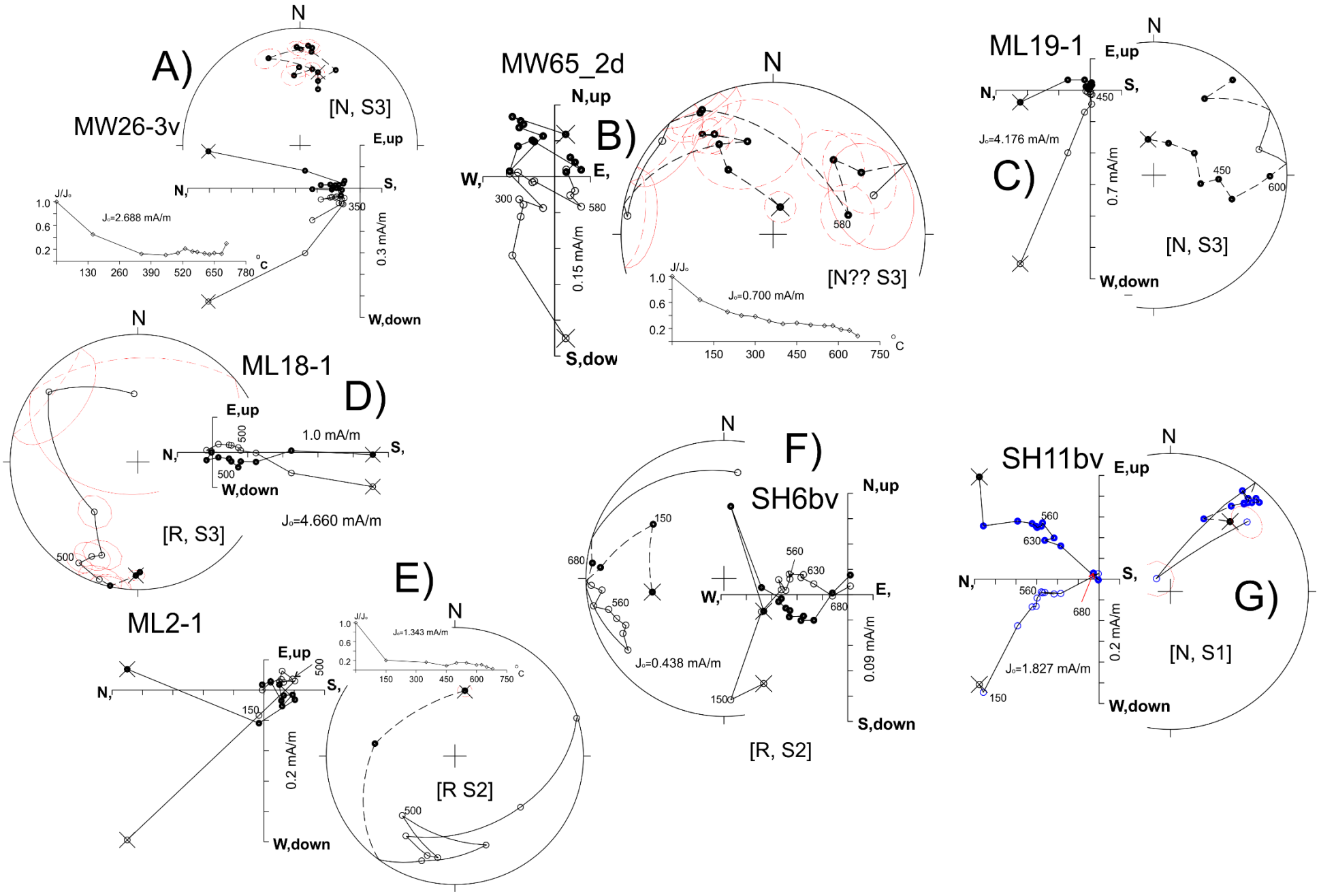
A)
MW26-3v
[N, S3]
N
E,up
N,
S,
W,down
J/J₀
J₀=2.688 mA/m
0.3 mA/m
B)
MW65_2d
N,up
W,
E,
S,dow
0.15 mA/m
[N?? S3]
J₀=0.700 mA/m
C)
ML19-1
N,
S,
E,up
W,down
J₀=4.176 mA/m
0.7 mA/m
[N, S3]
D)
ML18-1
E,up
N,
S,
W,down
1.0 mA/m
J₀=4.660 mA/m
[R, S3]
E)
ML2-1
E,up
N,
S,
W,down
J₀=1.343 mA/m
0.2 mA/m
[R S2]
F)
SH6bv
N,up
W,
E,
S,down
J₀=0.438 mA/m
0.09 mA/m
[R, S2]
SH11bv
E,up
N,
S,
W,down
J₀=1.827 mA/m
0.2 mA/m
[N, S1]
G)

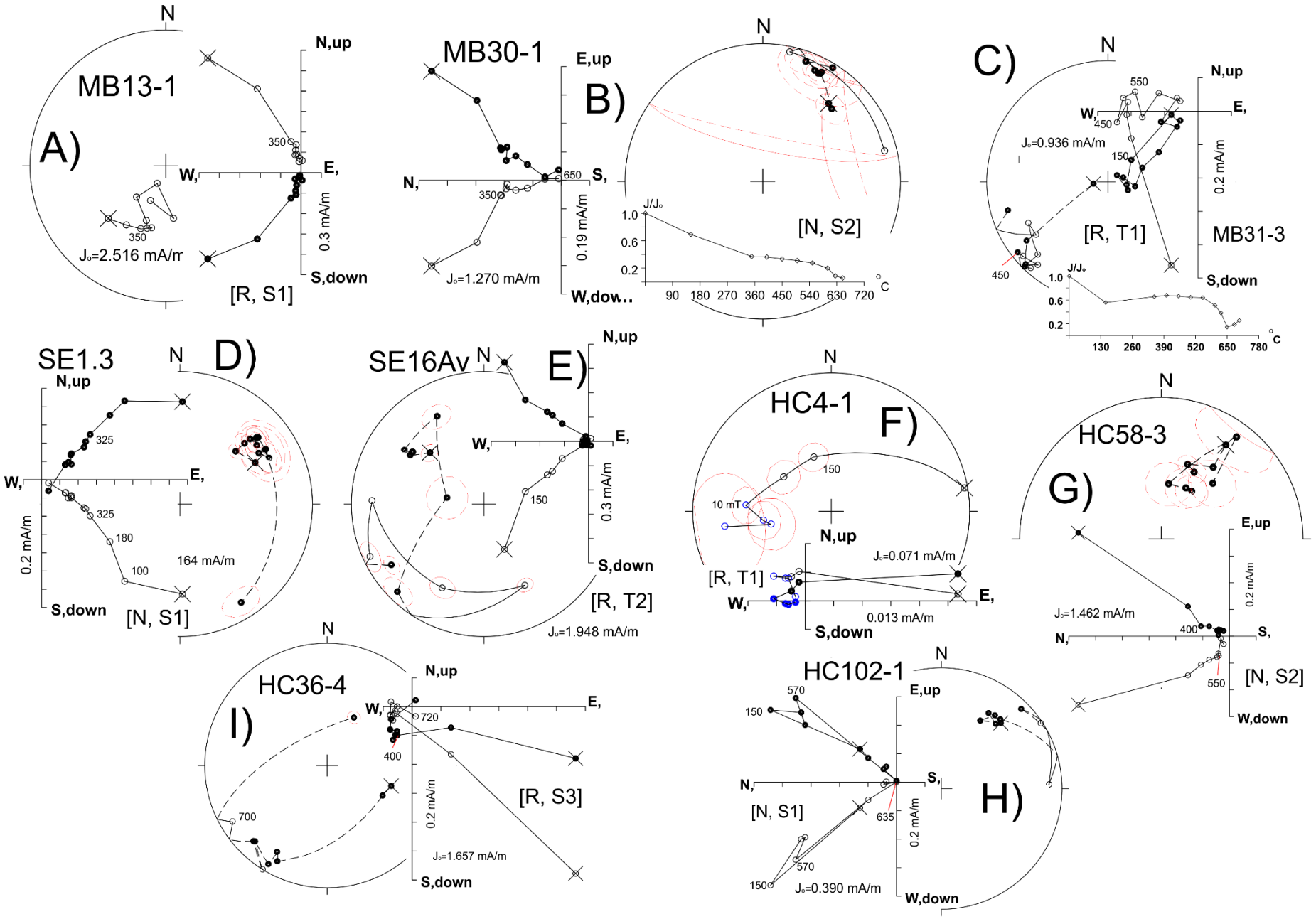
A)
MB13-1
N
N,up
E,
W,
S,down
0.3 mA/m
350
350
J₀=2.516 mA/m
[R, S1]
B)
MB30-1
N
E,up
N,
S,
W,down
650
350
0.19 mA/m
J₀=1.270 mA/m
J/J₀
1.0
0.6
0.2
90 180 270 360 450 540 630 720 °C
[N, S2]
C)
N
N,up
E,
W,
550
450
150
J₀=0.936 mA/m
0.2 mA/m
[R, T1]
MB31-3
S,down
450
J/J₀
1.0
0.6
0.2
130 260 390 520 650 780 °C
D)
SE1.3
N
N,up
W,
E,
325
325
180
100
164 mA/m
0.2 mA/m
S,down
[N, S1]
E)
SE16Av
N
N,up
W,
E,
150
0.3 mA/m
S,down
[R, T2]
J₀=1.948 mA/m
F)
HC4-1
N
150
10 mT
N,up
J₀=0.071 mA/m
[R, T1]
W,
E,
0.013 mA/m
S,down
G)
HC58-3
N
E,up
0.2 mA/m
J₀=1.462 mA/m
N,
400
S,
550
[N, S2]
W,down
I)
HC36-4
N
N,up
W,
E,
720
400
700
0.2 mA/m
[R, S3]
J₀=1.657 mA/m
S,down
H)
HC102-1
N
570
E,up
150
N,
S,
[N, S1]
635
570
150
0.2 mA/m
J₀=0.390 mA/m
W,down

Fig. S3.9 (previous page). Representative demagnetisation plots for the Seaton Mudstone and Haven Cliff Mudstone members and the Blue Anchor Fm. see preamble to Fig.S3.7 for plot and labelling details.

A) MB13-1 (47.59 m), reverse polarity (R) with ChRM component 350°C to origin {203°,-45°, -75°}. B) MB30-1 (0.29 m), normal polarity (N) with LT component NRM to 350°C {049°, 35°}and ChRM component 400-650°C {025°, 13°, 78°}. C) MB31-3 (2.08 m) reverse polarity (R) with LT component 150-550°C {033°, 62°} and a plane fitted between the 450°C and the origin {310°, -3°, -85°} defining the magnetisation direction. D) SE1.3 (15.47 m), normal polarity (N) with a weak/doubtful LT component 100-180°C {046°, 62°}, and strong ChRM between 325°C and the origin {053°, 27°, 71°}. E) SE16Av (9.69 m), with LT component NRM-150°C {331°, 53°} and a weak reverse polarity component defined by a great circle trend from NRM to origin {149°, 51°, -83°}. The strong intermediate component is a composite with positive inclination directed to the NW. F) HC4-1, grey-green mudstone (11.35 m, Blue Anchor Fm), reverse polarity, with LT component NRM-150°C {087°, 12°} and great circle trend from 10 mT to the origin {199°, 21°, -59°}. G) HC58.3, red-grey mottled mudstone (-25.5 m), normal polarity, with a strong LT component NRM-400°C {33, 17} and a ChRM 500°C to the origin {027°, 53°, 72°}. H) HC102-1 (-6.5 m) , normal polarity, LT component NRM-150°C (202°, -38°}, and a ChRM 570-635°C {040°, 29°, 86°}. I) HC36-4 (-27.7 m), reverse polarity, with a strong LT component NRM-400°C {086°, 53°} and a weak very high temperature ChRM, 700-720°C {232°, -25°, -76°}. The intermediate component is inferred as composite, shallow and directed to the SW.

Type/ section/ Unit	Dec(°)	Inc(°)	K/α_{95}(°)	Ns/Nl/Np	Reversal Test	G_O/G_C(°)	Plat/ Plong(°)	Dp/Dm (°)	A95 (min, max), %VGP_{45}
Salcombe Cliff (MS)									
Line fits$	29.8.0	25.9	20.5/5.4	35/37/0	Rc	5/11.3*	45.8/132.9	3.2/5.8	5.2 (2.9, 8.7), 0
GC means+	28.8	25.3	11.1/4.7	40/37/7	Rc	2.8/15.4	45.9/134.4	2.7/5.1	4.5 (2.7,8.0), 0
Dunscombe Cliff (MD)									
Line fits$	29.2	29.0	29.2/6.5	15/18/0	Rc	4.9/15*	47.7/132.5	3.9/2.7	6.9 (4.1, 14.9), 0
GC means+	28.0	30.0	16.4/5.3	18/18/6	Ro	3.7/21	48.8/133.6	3.3/5.9	6.2 (3.8, 13.3), 0
Strangman's Cove (MW)									
Line fits$	33.8	35.5	20.6/4.9	28/43/0	Rb	4.3/7.8*	49.1/123.7	3.3/5.7	5.8 (3.2, 10.0), 0
GC means+	34.3	37.2	11.4/3.5	44/43/33	Rb	4.4/8.1*	49.8/122.1	2.4/4.1	3.8 (2.6, 7.6), 3.6
Littlecombe Shoot west (ML)									
Line fits$	33.9	26.7	16.8/9.0	14/17/0	Ro	7.7/32	44.3/127.7	5.3/9.8	8.0 (4.2,15.6), 0
GC mean+	33.7	26.9	10.7/6.8	18/17/6	Ro	7.3/33	44.5/127.9	4.0/7.4	6.6 (3.8, 13.3), 10.7
Littlecombe Shoot east (SH)									
Line fits$	33.9	27.1	20.8/9.3	8/13/0	Ro	6.9/27	44.5/127.6	5.5/10/1	11.3 (5.2, 22.1), 0
GC mean+	31.8	32.8	10.6/7.3	10/13/6	Rc	9.5/17*	48.6/127.6	4.7/8.3	8.8 (4.8, 19.2), 0
Branscombe (MB)									
Line fits$	30.7	28.5	21.9/5.9	25/29/0	Rc	10.3/12.0*	46.8/130.9	3.6/6.5	6.0 (3.3, 10.8), 0
GC mean+	31.5	26.8	12.0/4.8	28/29/7	Rc	10.5/10.7*	45.5/130.6	2.8/5.2	5.2 (3.2, 10.0), 0
Seaton (SE)									
Line fits$	37.2	29.8	24.8/6.1	16/24/0	Rc	7.6/12.9*	44.3/122.7	3.7/6.8	5.6 (4.0, 14.3), 0
GC mean+	38.4	31.1	9.1/6.4	16/24/5	Rc	7.1/29	44.3/120.7	4.0/7.2	5.2 (4.0, 14.3), 0
Haven Cliff (HC)									
Line fits$	39.6	35.6	24.0/3.4	51/74/0	R-	8.3/8.0	44.0/126.6	2.3/3.9	3.5 (2.5, 6.9), 1.4
GC mean+	37.7	34.2	10.1/2.6	74/74/63	R-	12.4/9.9	44.1/129.4	1.7/3.0	3.0 (2.1, 5.4), 2.1
Formation Means:									
Branscombe Mudstone$,1	33.5	28.4	21.4/3.4	66/86/0	Rb	3.5/6.8	45.4/127.5	2.0/3.7	3.4 (2.2, 5.9), 0
Dunscombe Mudstone$	33.0	35.5	20.7/5.6	20/33/0	Rc	4.9/11.6	49.5/124.7	3.7/6.5	6.2 (3.6, 12.4), 0
Sidmouth Mudstone$	30.9	28.1	22.0/4.1	51/58/0	Rc	2.8/13.1	46.5/130.7	2.5/4.5	4.3 (2.5, 6.9), 0
Pennington Point Mb$	18.7	27.7	11.7/13.3	10/12/0	-	-	51.0/147.3	7.9/14.5	+10.8 (4.8, 19.2), -

Table S3.1. Directional means (with tectonic correction), reversal tests and VGP poles. +=great circle combined mean using method of McFadden & McElhinny (1988). $=conventional Fisher mean. 1= not including Haven Cliff data. Ns=number of levels (sites), Nl=number of specimens used with fitted

lines, and Np =number of specimens with great circle planes used in the determining the mean direction. α_{95}, Fisher 95% cone of confidence. k, Fisher precision parameter. G_O is the angular separation between the inverted reverse and normal directions, and Gc is the critical value for the reversal test. In the reversal test the Go/Gc values flagged with * indicate common K values, others not flagged have statistically different K-values for reverse and normal populations, in which case a simulation reversal test was performed. Plat and Plong are the latitude and longitude of the mean virtual geomagnetic pole[1]. For GC means reverse and normal means averaged using Fisher pooled mean (based on dispersion; Fisher et al. 1993), for line-fits by inverting the reverse set. Pennington Point and Sidmouth Mudstone means use data also from Hounslow & McIntosh (2003). A95 (min, max) = Fisher 95% confidence interval for VGP-based site mean (N_s sites), and $A95_{min}$ and $A95_{max}$ threshold values of Deenen et al. (2011). $\%VGP_{45}$= percent of samples yielding VGP latitude < |45|, as a reflection of the match to modern geomagnetic field models and palaeomagnetic data in which $\%VGP_{45}$ is a 3-4% (Cromwell et al. 2018). $\%VGP_{45}$ applies to all the section. Statistics determined with Pmagtool v.5 (Hounslow 2006).

Section S4: Virtual geomagnetic pole (VGP) data for the European mid and late Triassic

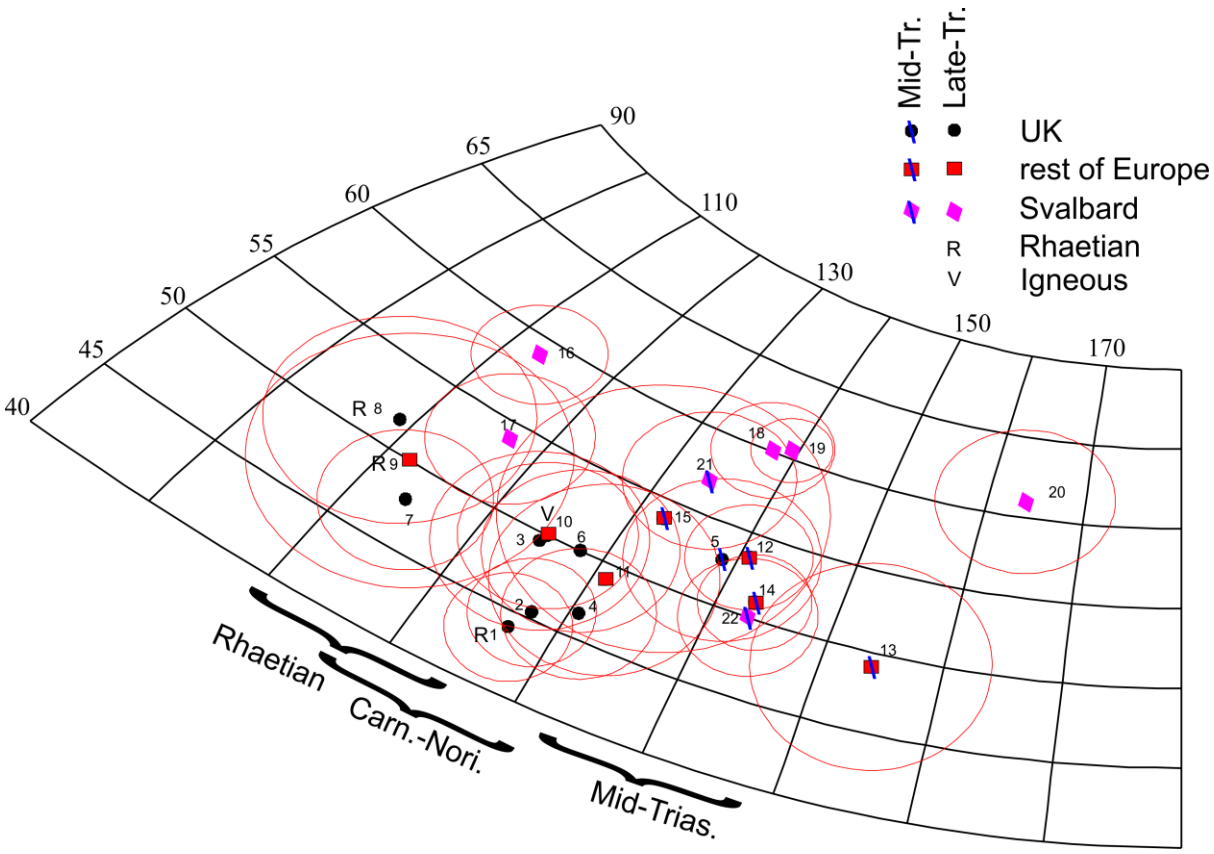

Fig. S4.1. VGP poles for stable Europe for the mid and late Triassic divided into source regions of the data and age intervals. The poles for the Devon coastal sections from this study are numbered 1 to 4, with 5 from Hounslow and McIntosh (2003). Apart from the poles from Svalbard these broadly indicate VGP latitude of ca. 50º, with the age intervals segmenting the data into larger (130-150º) and smaller VGP longitude. The poles are numbered according to Table S4.1.

Formation/Mb/Unit	α_{95}	Lat.	Long.	label	Pole ID
Haven Cliff section	3.4	44	126.6	L-MMG	1
Branscombe Mudstone Fm	3.4	45.4	127.5	L-MMG	2
Dunscombe Mudstone Fm	5.6	49.5	124.7	L-MMG	3
Sidmouth Mudstone Fm	4.1	46.5	130.7	L-MMG	4
Otter Sandstone Fm, Devon coast	5.1	52.8	138.8	M	5
Branscombe M. Fm, St Audrie' Bay	5.1	50	128	L-MMG	6
Branscombe M. Fm, St Audrie' Bay	4.4	47.9	114	L-MMG	7
Blue Anchor Fm, St Audrie' Bay	6.5	51.7	108.9	L-MMG	8
Rhaetian Sandstones	8	50	112	L	9
Sunhordland dykes (221± 5 Ma)	4.6	50	125	L	10
Gipskeuper red beds (Carnian)	6	49	131	L	11
Ladinian sediments, red dolomites	3.3	53.5	140.8	M	12
basal Anisian, Rot Fm	6.5	49.1	154.1	M	13
Polish Muscelkalk, Anisian	3	51	143	M	14
Edivetur Limestones, Anisian, Bulgaria	8.4	53.8	132.4	M	15
De Geerdalen Fm, Dalsnuten	3.1	59	113	S-L	16
Tschermakfjellet Fm, Dalsnuten	4.1	54	117	S-L	17
Nordstefjellet section, Hopen	3	60.1	137.6	S-L	18
Binnedalen section, Hopen	2	60.5	139.3	S-L	19
Tumlingodden, Wilhelmøya	4.5	61	163.8	S-L	20
Top Botneheia Fm, Milne_Edwardsfjellet	4.3	57	134	S-M	21
Botneheia Fm, Milne_Edwardsfjellet	3.7	50	143	S-M	22

Table 4.1. Triassic VGP poles for stable Europe. Label indicates category, M=mid Triassic, L=Late Triassic, S=from Svalbard, MMG=from Mercia Mudstone Group. Poles 1 to 4 from this work. 5=Hounslow and Mcintosh (2003). 6=Briden and Daniels (1999), 7-8=Hounslow et al. (2004).; 9,11=Edel and Duringer (1997); 10= Walderhaug et al. (1993); 12= Théveniaut _et al. (1992); 13=Szurlies (2007); 14= Nawrocki and Szulc (2000); 15= Muttoni et al. (2000). 16,17= Hounslow et al. (2007); 18-20= Hounslow et al (2022), 21-22=Hounslow et al. (2008).

Section S5: Reference magnetostratigraphic sections and the GPTS-B for the Norian and Rhaetian

The numbering of magnetochrons UT17 and UT18 (in main text Figs. 13, 15,16), has been changed from that given in Hounslow and Muttoni (2010), by upgrading the Newark magnetozone E12n (now UT17n) to a full magnetochron and down-grading the equivalent of E13r.1n (UT18r.1n) to a subchron. The marine composite for the Norian-Rhaetian boundary interval from Hounslow and Muttoni (2010) has been updated with new data (Fig. S5.1).

Magnetostratigraphic and U-Pb radiometric dating has given a clearer picture of the synchronicity between the eruption of the Central Atlantic Magmatic Province LIP, and events in the oceans near the Triassic-Jurassic boundary (Deenen et al. 2010, Whiteside et al. 2010; Olsen et al. 2011). Brief reverse polarity intervals are now seen to precede and follow the initial C^{13} isotopic excursion (Fig. S5.2), prior to the Triassic-Jurassic boundary (marked by *Psiloceras spaele* in the Hettangian GGSP at Kujoch; Schoene et al. 2011). Data from the Moenave Formation (Donohoo-Hurley et al. 2010) and Argana Basin (Deenen et al. 2010) was used to refine the magnetochrons UT25 to UT28 (Fig. S5.2) originally defined by Hounslow and Muttoni (2010). A Lower Jurassic, LJ chron numbering is

introduced (Fig. S5.2), with the placement of the magnetostratigraphy with respect to the Hettangian-Sinemurian boundary according to Ruhl et al. (2010). Kent et al. (2017) has proposed an alternative APTS for this interval based on the Newark-Hartford successions.

In addition, the Chinle Fm/Group in SW USA has a well-studied polarity dataset, with associated detrital zircon age dates which clearly dates it to the mid Norian. A composite magnetostratigraphy of the upper Chinle Fm is constructed and used in this work, and its source data and composite construction is outlined in the below section.

It has now been formally proposed that the GSSP for the Carnian-Norian boundary is placed in the Pizzo Mondello section at the first occurence of *Halobia austriaca,* which is within the lower part of magnetozone UT13n (PM5n at Pizzo Mondello), Hounslow et al. (2021).

S5.1 The Chinle Group/Fm magnetostratigraphy and U-Pb dates

Lithostratigraphic correlations between the various units of the upper Chinle Fm (some use this as a Group) in New Mexico, Arizona and Utah are problematic, and probably may not provide a particularly robust means of high-resolution correlation over large areas (Ramezani et al. 2011). This is fundamentally related to the complex fluvial system that the Chinle represents, and a number of unconformities which may sub-divide it (Heckert and Lucas 2002). Consequently, the magnetic polarity synthesis (SI Figs. S5.3, S5.4) has constructed magnetostratigraphy composites over smaller areas for comparison, based on; a) the Chama Basin (Zeigler and Geissman 2011) in northern New Mexico, b) San De Cristo Mts and Tucumcari Basin (Molina-Garza et al. 1996; Reeve and Helsley 1972; Zeigler and Geissman 2011) in eastern New Mexico, c) Petrified Forest National Park (PEFO) area in eastern Arizona (Steiner and Lucas 2000, Ziegler et al. 2017; Kent et al. 2019; Rasmussen et al. 2021). Sections S5.1.1 to S5.1.3 examine these regional records, and section S5.1.4 discusses their amalgamation in Fig. S5.4.

S5.1.1 Petrified Forest National Park (PEFO), Arizona

Biostratigraphy: The zone II/Zone III palynostratigraphic boundary (Litwin et al. 1991, refined by Baryani et al. 2018) in the PEFO is above the Rainbow Forest bed and within the Jim Camp Wash beds (Parker and Martz 2011; SI Fig S5.3) slightly below or at the level of the Adamanian - Revueltian vertebrate turnover (Baryani et al. 2018). This level has been correlated to the New Oxford-Lockatong – Lower Passaic Heidlersburg palynozone boundary in the Passaic Fm (Olsen et al. 2011; Lucas et al. 2012). A similar biostratigraphic correlation argument, but based on land vertebrate and conchostracan faunas has been proposed by Lucas et al. (2012) who correlate the bases of the Sonsela Member and the Passaic Formation, using specifically the miospore *Camerosporites veruccosus* which occurs in the Chinle Zone III assemblage from the PEFO (Parker and Martz 2011). This has a first occurrence (FO) in the base of the Passaic Fm (Warford- Graters members, in magnetozone E11; Lucas et al. 2012). In addition, the pollen *Perinopollenites elatoides* has been found in the Sonsela Sandstone in the base of zone III, which allows potential correlation of this interval to the mid Norian of the Germanic facies in Europe (Baryani et al. 2018). Contrastingly, Lucas et al. (2012) correlates the base of the Revueltian to the Warford Member of the Passaic Formation using vertebrate data (this is the mid part of magnetozone E11 in the Newark Supergroup).

Zircon U/Pb dates: An extensive and well documented re-evaluation of the lithostratigraphy of the Sonsela Member in the PEFO (Martz and Parker 2010; Parker and Martz 2011), has allowed a re-

evaluation of the magnetostratigraphic study of Steiner and Lucas (2000), along with more recent polarity data from outcrops (Ziegler et al. 2017) and the core through the PEFO succession (Kent et al. 2019). This allows the relationship between the magnetostratigraphy, the revised lithostratigraphy (Irmis et al. 2011; Parker and Martz 2011) and the zircon CA-ID TIMS U/Pb dates to be defined with greater confidence (Fig. S5.3). Based on the lithostratigraphy of Irmis et al. (2011) and the magnetostratigraphy of Zeigler and Geissman (2011), additional U-Pb dates from the Six Mile Canyon section and the Chama Basin can be related to the PEFO succession (Fig. S5.4). The detrital zircon age dates do represent substantial challenges in dating the age of deposition, since re-cycling of older zircons in the sand-prone units is probably an issue in the Sonsela Sandstone (Gehrels et al. 2020), which could have biased the zircon ages to older dates in the sandy units.

S5.1.2 Chama Basin, New Mexico

The main independent control on association between strata in the separate sub-basins of the Chinle Fm/Grp are the land vertebrate faunachrons (Lucas 2010), which broadly allow stratigraphic grouping of sections into the Adamanian, Revueltian and Apachean (left side of PEFO outcrop column in Fig. S5.4).

The Chama Basin composite (Fig S5.4) is based on the Coyote Amphitheatre section for the youngest units and the Abuiquiu Dam section for the Poleo Fm (Zeigler and Geissman 2011). The placement of the Hayden Quarry section radiometric date (i.e., 211.9 Ma) onto the Chama Basin magnetostratigraphy uses the lithostratigraphic correlation of Irmis et al. (2011). The roughly equal duration magnetozones in the Salitral Fm (Zeigler and Geissman 2011) is unlike the Norian, and in terms of relative magnetozone duration, is most similar to the polarity pattern in parts of the Carnian (see main text), so is not included in Fig. S5.4.

The reverse polarity dominated composite Chama Basin composite section through the Poleo Fm and Petrified Forest Mb is unlike the mixed polarity seen in the Revueltian LVF age strata from the PEFO, so may represent the reverse polarity intervals in the PEFO core PF4r and PF3r (Fig. S5.4). The uppermost normal polarity zone in the upper siltstone member (Chama Basin column) is likely related to that in the basal Redonda Mb, as proposed by Ziegler and Geissman (2011). The Hayden Quarry section U-Pb date (211.9 Myr) is correlated to near the base of the Petrified Forest Member in the Chama Basin (Irmis et al. 2011; Zeigler and Geissman 2011). The ~215 Ma date from Dickinson and Gehrels (2008) from the Poleo Fm suggests this interval is probably PF4r (Fig. S5.4). The correlation of the inferred ‘Rock Point’ unit in the Chama Basin to the Redonda Fm in eastern New Mexico follows Zeigler and Geissman (2011).

S5.1.3 Sangre de Cristo Mountains and Tucumcari Basins, New Mexico

Well constrained correlations between the Redonda Fm in the San De Cristo and Tucumcari basins are not possible. The upper part of the Redonda Fm (E. New Mexico column in Fig. S5.4) appears to be normal polarity dominated (Reeve and Helsley 1972; Molina-Garza et al. 1996), whereas the mid parts appear reverse to mixed polarity dominated (Fig. S5.4). There are differences between the magnetostratigraphy of the closby Mesa Redonda and Mesa Luciana sections near Tucumcari (Reeve and Helsley 1972; Ziegler and Geissman 2011), and the Redonda Mb composite reflects this uncertainty (due to differences in section thickness, and magnetic polarity in the lowermost and upper-most parts of the Redonda Fm in these sections). The Sebastian Canyon section of the Redonda Fm (Molina-Garza et al. 1996) is not shown due to its low-resolution sampling. The Revueltian and

Adamanian units in these basins are largely placed onto the composite chart (Fig. S5.4), using the land vertebrate faunachron data (Lucas 2010). Relying on the lithostratigraphic equivalence of the Trujillo and Poleo formations allows a tentative correlation of these sections.

S5.1.4. Construction of the upper Chinle Fm composite

The construction of the polarity composite is to a large extent guided by the many zircon U/Pb dates, along with the reference sections through the upper Chinle provided by the PEFO outcrops and core (Figs. S5.3, S5.4). The magnetostratigraphy in the Blue Mesa Mb seems well defined with three magnetic polarity studies in this interval (three PEFO colunns in Fig. S5.4). The Chinle composite CC1 to CC4 magnetozones are based on the PFNP-1A core (Fig. S5.4). From the PEFO, the Sonsela Sandstone is dominated by normal polarity, yet the apparent age equivalent units in the Chama Basin and Sangre de Cristo Mountains are reverse polarity dominated (except in the Tucamcari Basin (Garita Creek); Fig. S5.4). Substantial detrital U/Pb age differences of the Sonsela Sandstone are a feature of its regional occurrence (Marsh et al. 2019). The U/Pb dates in the PEFO both from outcrop and core, at face value, suggest a condensed (or hiatus) internal at around the position of the Rainbow/Jasper Forest bed (Fig. S5.3). A regional hiatus (TR4a or TR4b) in the lower or basal Sonsela Sandstone has also been widely inferred (Heckert and Lucas 2002; Tanner and Lucas 2006), and a change at around the Jasper Forest bed is coincident with a major climatic shift (Nordt et al. 2015), which may be the driver for any condensed interval or hiatus. We infer that further east in the New Mexico successions this hiatus is better expressed and has removed much of the lower part of the Sonsela Sandstone (i.e. better preserved in the PEFO), so that magnetozone CC5n is missing (e.g. in the Chama Basin), and the reverse polarity dominance as seen in E. New Mexico sections at this level largely represent PF4r and PF3r in the PEFO outcrops and core. Substantial differences in thickness of reverse and normal intervals in CC6 and CC7 also seem to be a feature of the Petrified Forest Mb and its equivalents which perhaps relate to the frequency of palaeosols in this member. The Redonda Mb is widely inferred to be largely Rhaetian in age, based on vertebrates and conchostracans (Lucas et al. 2012), and this is largely confirmed by inference based on magnetostratigraphy (Fig. S5.4 and main text).

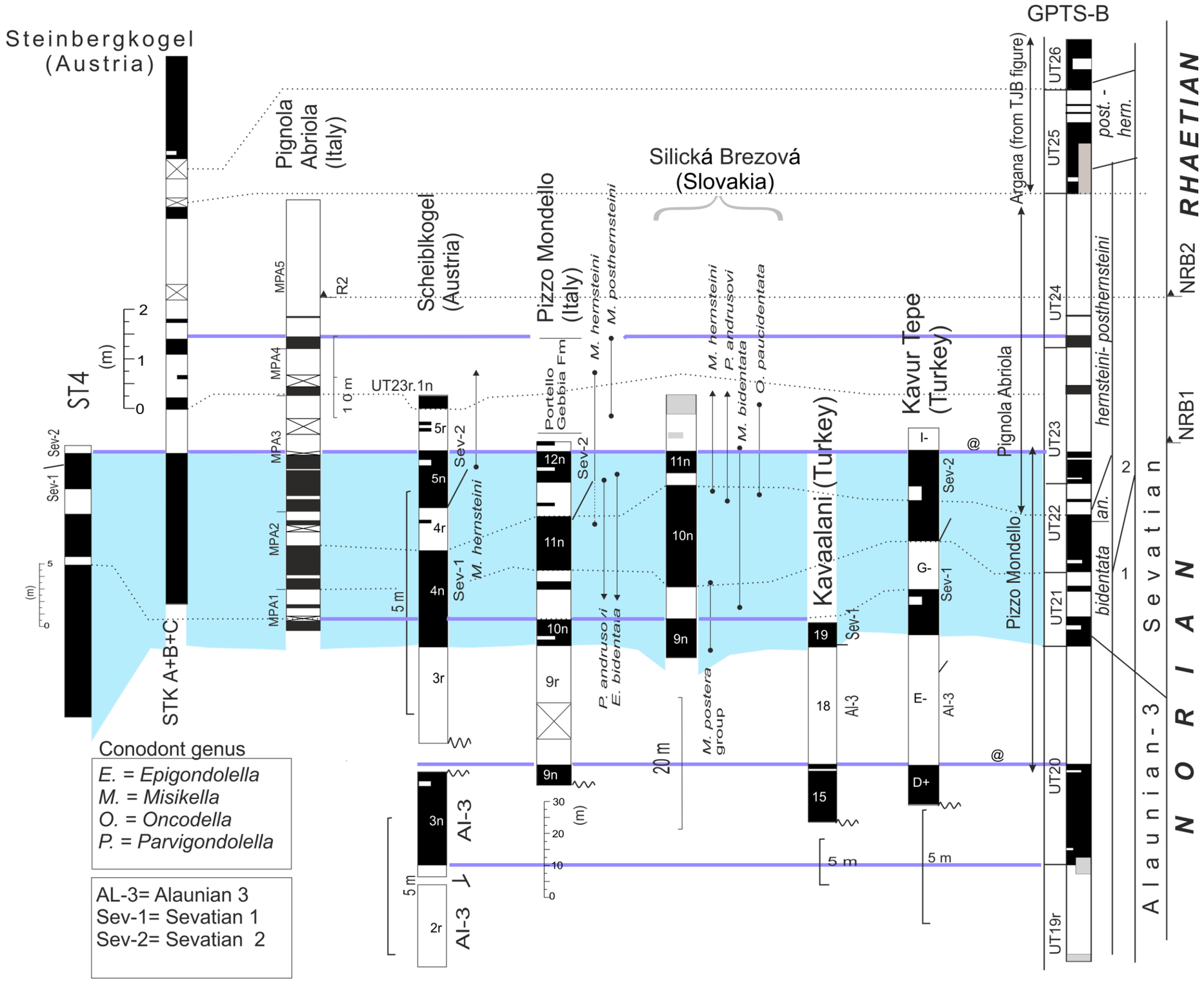

Fig. S5.1. The construction of the magnetostratigraphy around the Norian-Rhaetian boundary using marine sections with biostratigraphy. This is based on Fig. 10 in Hounslow and Muttoni (2010), but with the addition of new data from Steinbergkogel of Hüsing et al. (2011) and Pignola Abriola of Maron et al. (2015) and Bertinelli-et al. (2016). The two proposed options for the base of the Rhaetian are NRB1 and NRB2 (Bertinelli et al. 2016; Galbrun et al. 2020). The conodont zones are those of Rigo et al (2018), but with the contentious Rhaetian boundary interval shown as a conodont range. See Hounslow and Muttoni (2010) for source of other data in this figure. The Sevatian 1 and 2 interval uses the concepts used with the original magnetostratigraphic source data.

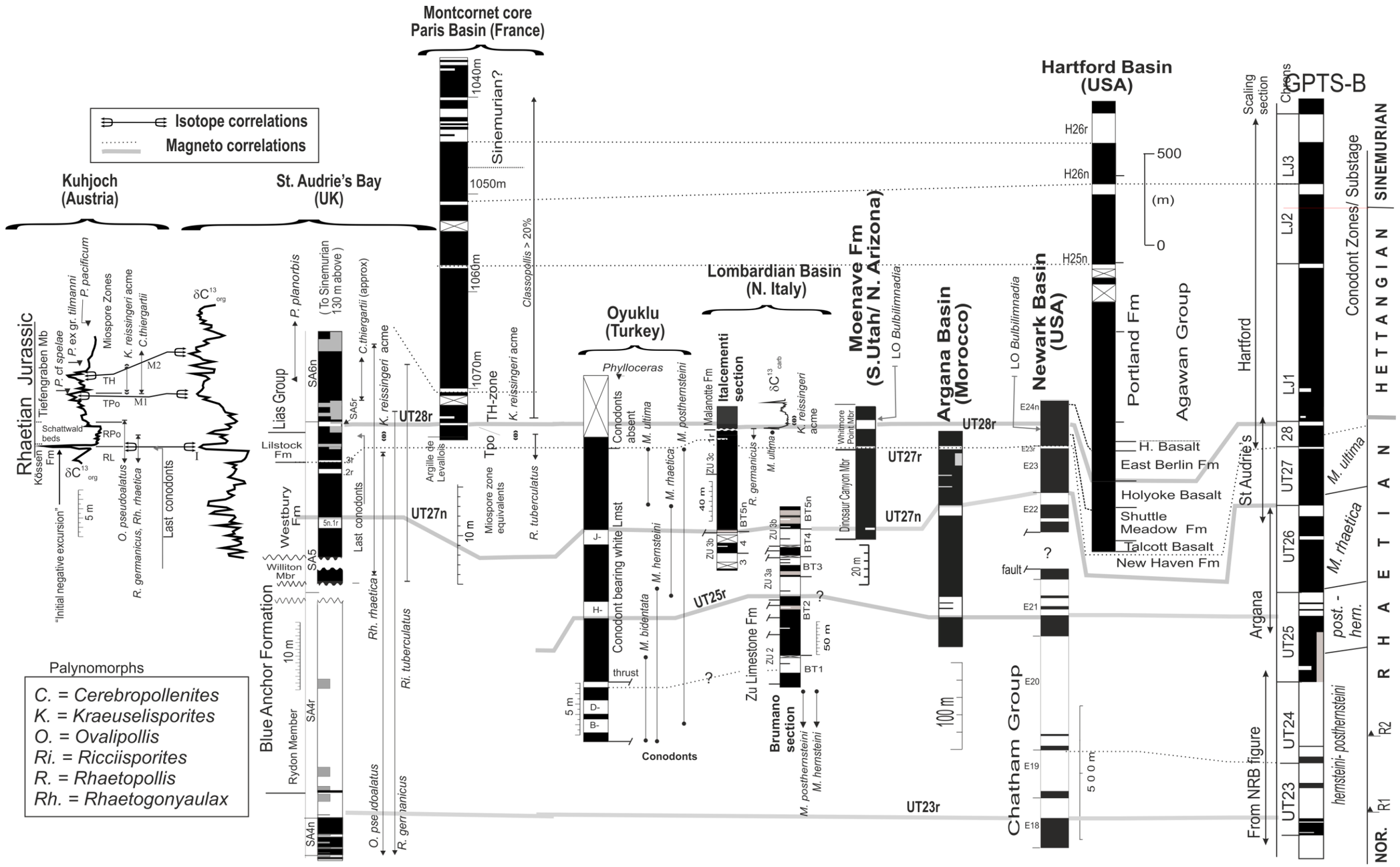

Fig. S5.2. Magnetostratigraphy of the Rhaetian-Hettangian transition modified from Hounslow and Muttoni (2010) by addition of data from the Moenave Fm (Donohoo-Hurley et al. 2010) and Argana Basin data (Deenan et al. 2010). Source details for other section data in Hounslow and Muttoni (2010). Main scaling anchors are UT23r, UT25r, UT27n, UT28r, LJ2n, LJ3r. Subsidiary scaling anchor UT27r. Based on the Italcementi and Brumano sections the interval UT25n- UT26r may be more complex (Maron et al. 2019, show very similar correlations) than is shown in the Newark Supergroup E21-E22, so an uncertain interval is inserted at the fault in the Newark core.

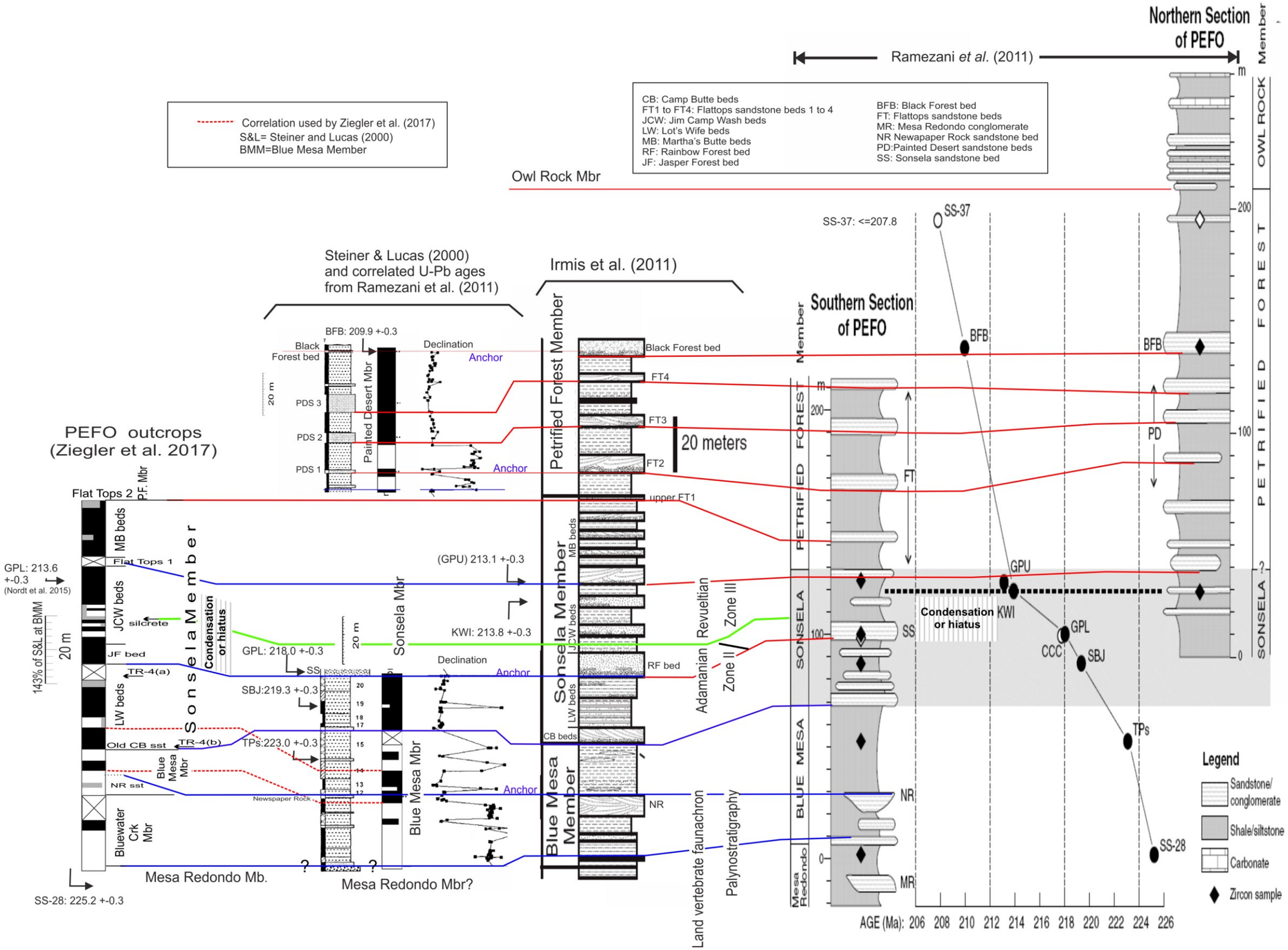

Fig. S5.3. Upper Chinle Formation lithostratigraphic columns used by the two main radiometric dating studies on outcrops in the Petrified Forest National Park (PEFO, Arizona), illustrating how the U-Pb dates (Irmis et al. 2011; Ramezani et al. 2011; Nordt et al. 2015) can be correlated to the PEFO outcrop magnetostratigraphy (Steiner and Lucas 2000; Ziegler et al. 2017), and biostratigraphy (Parker and Martz 2011; Baranyi et al. 2018) and hence their placement on Fig. S5.4. Member boundaries in blue. Sections from the CA-IDTIMS U/Pb dating studies have been scaled using the top of the Newspaper Rock Sandstone and the base of the Black Forest bed. Green correlation line is the Adamanian-Revueltian boundary.

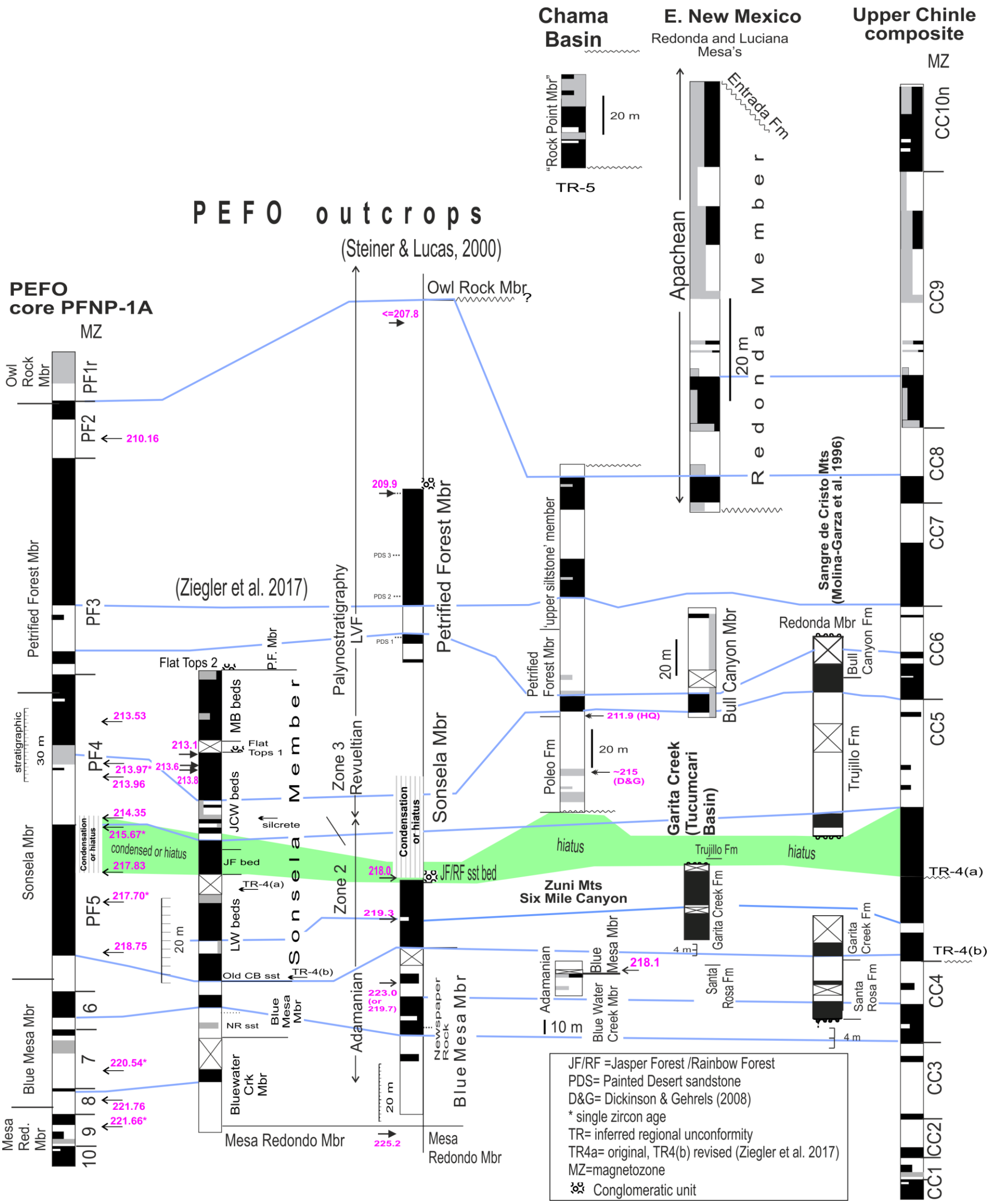

Fig. S5.4. Correlations between the various sections with magnetostratigraphy from the Chinle Fm/Group. The data from the Petrified Forest National Park (PEFO) is related to the reference section in the PEFO core 1a, and its associated detrital zircon dates (Kent et al. 2019; Rasmussen et al. 2021). The magnetic polarity stratigraphy from the outcrops in the PEFO (Steiner and Lucas 2000) indicates a close similarity the Blue Mesa, Sonsela and Petrified Forest members in the cores. Sources of other data for the Chinle Group are Reeve and Helsley (1972), Molina-Garza et al. (1996 2003), Zeigler and Geissman (2010). These sources have all been re-drawn with the same style for uncertain intervals and sampling gaps. See the text for discussion of these relationships.

Supplementary References

Baranyi, V., Reichgelt, T., Olsen, P.E., Parker, W.G. and Kürschner, W.M. 2018. Norian vegetation history and related environmental changes: New data from the Chinle Formation, Petrified Forest National Park (Arizona, SW USA). *GSA Bulletin*, 130, 775-795.

Baranyi, V., Miller, C.S., Ruffell, A., Hounslow, M.W. and Kürschner, W.M. 2019. A continental record of the Carnian Pluvial Episode (CPE) from the Mercia Mudstone Group (UK): palynology and climatic implications. *Journal of the Geological Society*, 176, 149-166.

Bertinelli, A., Casacci, M., Concheri, G., Gattolin, G., Godfrey, L., Katz, M.E., Maron, M., Mazza, M., Mietto, P., Muttoni, G. and Rigo, M. 2016. The Norian/Rhaetian boundary interval at Pignola-Abriola section (Southern Apennines, Italy) as a GSSP candidate for the Rhaetian Stage: an update. *Albertiana*, 43, 5-18.

Briden, J.C. and Arthur, G.R., 1981. Precision of measurement of remanent magnetization. *Canadian Journal of Earth Sciences*, 18, 527-538.

Briden, J.C. and Daniels, B.A. 1999. Palaeomagnetic correlation of the Upper Triassic of Somerset, England, with continental Europe and eastern North America. *Journal of the Geological Society*, 156, 317-326.

Creer K.M. 1955. *A preliminary survey of certain rocks in England and Wales*. PhD. Thesis Cambridge, 203pp.

Creer, K.M. 1957. V. The remanent magnetization of unstable Keuper Marls. Philosophical *Transactions of the Royal Society of London. Series A, Mathematical and Physical Sciences*, 250, 130-143.

Creer, K.M. 1959. AC demagnetization of unstable Triassic Keuper Marls from SW England. *Geophysical Journal of the Royal Astronomical Society*, 2, 261-275.

Creer, K.M. 1961. Superparamagnetism in red sandstones. *Geophysical Journal of the Royal Astronomical Society,* **5**, 16-28.

Creer, K.M. 1962. On the origin of the magnetization of red beds. *Journal of geomagnetism and geoelectricity*, **13**, 86-100.

Cromwell, G., Johnson, C.L., Tauxe, L., Constable, C.G. and Jarboe, N.A. 2018. PSV10: A global data set for 0–10 Ma time-averaged field and paleosecular variation studies. *Geochemistry, Geophysics, Geosystems*, 19, 1533-1558.

Deenen, M.H.L., Ruhl, M., Bonis, N.R. Krijgsman, W., Kuerschner W.M. Reitsma M. and van Bergen M.J. 2010. A new chronology for the end-Triassic mass extinction. *Earth and Planetary Science Letters* 291**,** 113–125.

Deenen, M.H., Langereis, C.G., van Hinsbergen, D.J. and Biggin, A.J. 2011. Geomagnetic secular variation and the statistics of palaeomagnetic directions. *Geophysical Journal International*, 186, 509-520.

Dickinson, W.R. and Gehrels, G.E. 2008. U-Pb ages of detrital zircons in relation to paleogeography: Triassic paleodrainage networks and sediment dispersal across southwest Laurentia. *Journal of Sedimentary Research*, 78, 745-764.

Donohoo-Hurley, L.L., Geissman, J.W. and Lucas, S.G. 2010. Magnetostratigraphy of the uppermost Triassic and lowermost Jurassic Moenave Formation, western United States: Correlation with strata in the United Kingdom, Morocco, Turkey, Italy, and eastern United States. *GSA Bulletin, 122*, 2005-2019.

Duff, B.A. 1979. Peaked thermomagnetic curves for hematite-bearing rocks and concentrates. *Physics of the Earth and Planetary Interiors*, 19, 1-4.

Edel, J.B. and Duringer, P.H. 1997. The apparent polar wander path of the European plate in Upper Triassic-Lower Jurassic times and the Liassic intraplate fracturing of Pangaea: new palaeomagnetic constraints from NW France and SW Germany. *Geophysical Journal International*, 128, 331-344.

Edwards, R.A. and Gallois, R.W., 2004. *Geology of the Sidmouth district: a brief explanation of the geological map sheets 326 and 340 Sidmouth*. British Geological Survey, HMSO.

Fisher, N.I., Lewis, T. and Embleton, B.J., 1993. *Statistical analysis of spherical data*. Cambridge University Press, Cambridge.

France, D.E. and Oldfield, F. 2000. Identifying goethite and hematite from rock magnetic measurements of soils and sediments. *Journal of Geophysical Research: Solid Earth,* 105, 2781-2795.

Galbrun, B., Boulila, S., Krystyn, L., Richoz, S., Gardin, S., Bartolini, A. and Maslo, M. 2020. " Short" or" long" Rhaetian? Astronomical calibration of Austrian key sections. *Global and Planetary Change*, 192, doi.org/10.1016/j.gloplacha.2020.103253.

Gallois, R.W. 2003. The distribution of halite (rock-salt) in the Mercia Mudstone Group (mid to late Triassic) in south-west England. *Geoscience in south-west England,* 10, 383-389.

Gallois, R.W. and Porter, R.J. 2006. The stratigraphy and sedimentology of the Dunscombe Mudstone Formation (late Triassic) of south-west England. *Geoscience in south-west England,* 11, 174-182.

Gehrels, G., Giesler, D., Olsen, P., Kent, D., Marsh, A., Parker, W., Rasmussen, C., Mundil, R., Irmis, R., Geissman, J. and Lepre, C. 2020. LA-ICPMS U–Pb geochronology of detrital zircon grains from the Coconino, Moenkopi, and Chinle formations in the Petrified Forest National Park (Arizona). *Geochronology*, 2, 257-282.

Heckert, A.B. and Lucas, S.G. 2002. Revised Upper Triassic stratigraphy of the Petrified Forest National Park, Arizona, USA. *In:* Heckert, A.B., and Lucas, S.G., eds., *Upper Triassic Stratigraphy and Paleontology*, *New Mexico Museum of Natural History and Science Bulletin*, 21, 1-36.

Hounslow, M.W. and McIntosh, G. 2003. Magnetostratigraphy of the Sherwood Sandstone Group (Lower and Middle Triassic), south Devon, UK: detailed correlation of the marine and non-marine Anisian. *Palaeogeography, Palaeoclimatology, Palaeoecology*, 193, 325-348.

Hounslow, M.W., Posen, P.E. and Warrington, G. 2004. Magnetostratigraphy and biostratigraphy of the Upper Triassic and lowermost Jurassic succession, St. Audrie's Bay, UK. *Palaeogeography, Palaeoclimatology, Palaeoecology*, 213, 331-358.

Hounslow, M.W., Hu, M., Mørk, A., Vigran, J.O., Weitschat, W. and Orchard, M.J. 2007. Magneto-biostratigraphy of the Middle to Upper Triassic transition, central Spitsbergen, arctic Norway. *Journal of the Geological Society*, 164, 581-597.

Hounslow, M.W., Hu, M., Mørk, A., Weitschat, W., Vigran, J.O., Karloukovski, V. and Orchard, M.J. 2008. Intercalibration of Boreal and Tethyan time scales: the magnetobiostratigraphy of the Middle Triassic and the latest Early Triassic from Spitsbergen, Arctic Norway. *Polar Research,* 27, 469-490.

Hounslow, M.W. and Muttoni, G. 2010. The geomagnetic polarity timescale for the Triassic: linkage to stage boundary definitions. *In:* Lucas, S.G. (ed) *The Triassic timescale*, *Geological Society, London, Special Publications*, 334, 61-102.

Hounslow, M.W. McKie, T. and Ruffell, A,H. 2012. Permian and Late Triassic post-orogenic collapse and rifting, arid deserts, evaporating seas and mass extinctions. *In:* Woodcock, N. and Strachan, R.(eds). *Geological history of Britain and Ireland.* Wiley-Blackwell, 2nd edn. 299-321.

Hounslow, M.W., Bachmann, G.H., Balini, M., Benton, M.J. Carter, E.S., Konstantinov, A.G., Golding, M.L., Krystyn, L., Kürschner, W., Lucas, S.G., McRoberts, C.A., Muttoni, G., Nicora, A., Onoue, T., Orchard, M.J., Ozsvárt, P., Paterson, N.W., Richoz, S., Manuel Rigo, M., Sun, Y., Tackett, L.S., Kağan Tekin, U., Wang, Y., Zhang, Y., and Zonneveld. J.-P. 2021. The case for the Global Stratotype Section and Point (GSSP) for the base of the Norian Stage. *Albertiana*, 46, 25–57 https://albertiana-sts.org/wp-content/uploads/2021/12/46-4_Hounslow_etal_2021.pdf

Hounslow, M.W., Harris, S., Karloukovski, V. and Mørk, A. 2022. Geomagnetic polarity and carbon isotopic stratigraphic assessment of the late Carnian-earliest Norian in Svalbard: evidence for a major hiatus and improved Boreal to Tethyan correlation. *Norwegian Journal of Geology*, 102. https://njg.geologi.no/images/NJG_articles/220409_Hounslow.pdf.

Hüsing, S.J. Deenen, M.H.L., Koopmans, J.G. and Krijgsman, W. 2011. Magnetostratigraphic dating of the proposed Rhaetian GSSP at Steinbergkogel (Upper Triassic Austria): Implications for the Late Triassic time scale. *Earth and Planetary Science Letters* 302**,** 203-216.

Irmis, R.B, Mundil, R., Martz, J.W. and Parker, W.G. 2011. High resolution U-Pb ages from the Upper Triassic Chinle Fm (New Mexico, USA) support a diachronous rise of dinosaurs. *Earth and Planetary Science Letters,* 309, 258-267.

Kent, D.V., Olsen, P.E. and Muttoni, G. 2017. Astrochronostratigraphic polarity time scale (APTS) for the Late Triassic and Early Jurassic from continental sediments and correlation with standard marine stages. *Earth-Science Reviews,* 166, 153-180.

Kent, D.V., Olsen, P.E., Lepre, C., Rasmussen, C., Mundil, R., Gehrels, G.E., Giesler, D., Irmis, R.B., Geissman, J.W. and Parker, W.G. 2019. Magnetochronology of the entire Chinle Formation (Norian age) in a scientific drill core from Petrified Forest National Park (Arizona, USA) and implications for regional and global correlations in the Late Triassic. *Geochemistry, Geophysics, Geosystems*, 20, 4654-4664.

Litwin, R. J, Traverse, A. and Ash, S. R. 1991. Preliminary palynological zonation of the Chinle Formation, southwestern U.S.A., and its correlation to the Newark Supergroup (eastern USA). *Review of Palaeobotany and Palynology,* 68, 269–87.

Lucas, S.G. 2010.The Triassic timescale based on non marine tetrapod biostratigraphy and biochronology *In:* Lucas, S.G. (ed). *The Triassic timescale*, *Special Publication of the Geological Society*, 334, 447-500.

Lucas, S.G. Tanner, L.H. Kozur, H.W., Weems, R.E. and Heckert, A.B. 2012. The late Triassic timescale: Age and correlation of the Carnian-Norian boundary. *Earth- Science Reviews*, 114, 1–18.

Maher, B.A., Karloukovski, V.V. and Mutch, T.J. 2004. High-field remanence properties of synthetic and natural submicrometre haematites and goethites: significance for environmental contexts. *Earth and Planetary Science Letters*, 226, 491-505.

Maron, M., Muttoni, G., Rigo, M., Gianolla, P. and Kent, D.V. 2019. New magnetobiostratigraphic results from the Ladinian of the Dolomites and implications for the Triassic geomagnetic polarity timescale. *Palaeogeography, Palaeoclimatology, Palaeoecology*, 517, 52-73.

Maron, M., Rigo, M., Bertinelli, A., Katz, M.E., Godfrey, L., Zaffani, M. and Muttoni, G. 2015. Magnetostratigraphy, biostratigraphy, and chemostratigraphy of the Pignola-Abriola section: New constraints for the Norian-Rhaetian boundary. *GSA Bulletin*, 127, 962-974.

Marsh, A.D., Parker, W.G., Stockli, D.F. and Martz, J.W. 2019. Regional correlation of the Sonsela Member (Upper Triassic Chinle Formation) and detrital U-Pb zircon data from the Sonsela Sandstone bed near the Sonsela Buttes, northeastern Arizona, USA, support the presence of a distributive fluvial system. *Geosphere*, 15, 1128-1139.

Martz, J.W. and Parker, W.G. 2010. Revised lithostratigraphy of the Sonsela Member (Chinle Formation, Upper Triassic) in the southern part of Petrified Forest National Park, Arizona. *PLoS One,* 5 (e9329), 1–26.

McFadden, P.L. and McElhinny, M.W. 1988. The combined analysis of remagnetization circles and direct observations in palaeomagnetism. *Earth and Planetary Science Letters*, 87, 161-172.

McFadden, P.L. and McElhinny, M.W. 1990. Classification of the reversal test in palaeomagnetism. *Geophysical Journal International*, 103, 725-729.

Molina-Garza, R.S., Geissman, J.W. and Lucas, S.G. 2003. Paleomagnetism and magnetostratigraphy of the lower Glen Canyon and upper Chinle Groups, Jurassic- Triassic of northern Arizona and northeast Utah. *Journal of Geophysical Research* 108, doi: 10.1029/2002JB001909.

Molina-Garza, R.S., Geissman, J.W., Lucas, S.G. and Van der Voo, R. 1996. Palaeomagnetism and magnetostratigraphy of Triassic strata in the Sangre de Cristo Mountains and Tucumcari Basin, New Mexico, U.S.A. *Geophysical Journal International* 124, 935-953.

Muttoni, G., Gaetani, M., Budurov, K., Zagorchev, I., Trifonova, E., Ivanova, D., Petrounova, L. and Lowrie, W. 2000. Middle Triassic paleomagnetic data from northern Bulgaria: constraints on Tethyan magnetostratigraphy and paleogeography. *Palaeogeography, Palaeoclimatology, Palaeoecology*, 160, 223-237.

Nawrocki, J. and Szulc, J. 2000. The Middle Triassic magnetostratigraphy from the Peri-Tethys basin in Poland. *Earth and Planetary Science Letters*, 182, 77-92.

Nordt, L., Atchley, S. and Dworkin, S. 2015. Collapse of the Late Triassic megamonsoon in western equatorial Pangea, present-day American Southwest. *GSA Bulletin*, 127, 1798-1815.

Newell, A.J. 2018a. Evolving stratigraphy of a Middle Triassic fluvial-dominated sheet sandstone: The Otter Sandstone Formation of the Wessex Basin (UK). *Geological Journal*, 53, 1954-1972.

Newell, A.J. 2018b. Rifts, rivers and climate recovery: A new model for the Triassic of England. *Proceedings of the Geologists' Association*, 129, 352-371.

Olsen, P.E., Kent, D.V. and Whiteside, J.H. 2011. Implications of the Newark Supergroup-based astrochronology and geomagnetic polarity time scale (Newark-APTS) for the tempo and mode of the early diversification of the Dinosauria. *Earth and Environmental Science Transactions of the Royal Society of Edinburgh,* 101, 1–33.

Parker W.G and Martz, J.W. 2011. The Late Triassic (Norian) Adamanian– Revueltian tetrapod faunal transition in the Chinle Formation of Petrified Forest National Park, Arizona. *Earth and Environmental Science Transactions of the Royal Society of Edinburgh*, 101, 231–260.

Ramezani, J., Bowring, S.A., Martin,Ramezani, J., Hoke, G.D., Fastovsky, D.E. Bowring, S.A., Therrien, F., Dworkin, S.I., Atchley, S.C. and Nordt, L.C. 2011. High-precision U-Pb zircon geochronology of the Late Triassic Chinle Fm, Petrified Forest National Park (Arizona, USA): Temporal constraints on the early evolution of dinosaurs. *Geol. Soc. America Bulletin,* 123, 2142-2159.

Rasmussen, C., Mundil, R., Irmis, R.B., Geisler, D., Gehrels, G.E., Olsen, P.E., Kent, D.V., Lepre, C., Kinney, S.T., Geissman, J.W. and Parker, W.G. 2021. U-Pb zircon geochronology and depositional age models for the Upper Triassic Chinle Formation (Petrified Forest National Park, Arizona, USA): Implications for Late Triassic paleoecological and paleoenvironmental change. *Geol. Soc. America Bulletin*, 133, 539-558.

Reeve, S.C. and Helsley, C.E. 1972. Magnetic reversal sequence in the upper part of the Chinle Formation, Montoya, New Mexico. *Geological Society of America Bulletin,* 83, 3795-3812.

Rigo, M., Mazza, M., Karádi, V. and Nicora, A. (2018). New Upper Triassic Conodont Biozonation of the Tethyan Realm. *In:* Tanner, L. (eds) *The Late Triassic World. Topics in Geobiology*, 46. 189-235, Springer, Cham. https://doi.org/10.1007/978-3-319-68009-5_6.

Ruhl, M., Deenen, M.H.L., Abel, H.A., Bonis, N.R., Krijgsman, W. and Kürschner, W.M. 2010. Astronomical constraints on the duration of the early Jurassic Hettangian stage and recovery rates following the end-Triassic mass extinction (St Audrie's Bay/East Quantoxhead, UK). *Earth and Planetary Science Letters* 295, 262–276.

Schoene, B., Guex, J., Bartolini, A., Schaltegger, U. and Blackburn, T.J. 2011. Correlating the end-Triassic mass extinction and flood basalt volcanism at the 100ka level. *Geology* 38, 387-390.

Schwarz, E.J. 1968. Thermomagnetic analysis of some red beds. *Earth and Planetary Science Letters*, 5, 333-338.

Shive, P.N. and Diehl, J.F. 1977. Thermomagnetic analysis of natural and synthetic hematite. *Geophysical Research Letters*, 4, 159-162.

Steiner, M.B. and Lucas, S.G. 2000. Palaeomagnetism of the late Triassic Petrified Forest Fm, Chinle Group, western United States: Further evidence of 'large' rotation of the Colorado Plateau. *Journal of Geophys. Res*., 105, 25791-25808.

Szurlies, M. 2007. Latest Permian to Middle Triassic cyclo-magnetostratigraphy from the Central European Basin, Germany: Implications for the geomagnetic polarity timescale. *Earth and Planetary Science Letters,* 261, 602-619.

Talbot, M., Holm, K. and Williams, M. 1994. Sedimentation in low-gradient desert margin systems: A comparison of the Late Triassic of northwest Somerset (England) and the late Quaternary of east central Australia. *In:* Rosen, M.R. (ed). *Paleoclimate and basin evolution of playa systems*, *Geol. Soc of America special paper,* 289, 97-118,

Tanner, L.H. and Lucas, S.G. 2006, Calcareous paleosols of the Upper Triassic Chinle Group, Four Corners region, southwestern United States: Climatic implications. *In:* Alonso-Zarza, A.M. and Tanner, L.H., (eds), *Paleoenvironmental record and applications of calcretes and palustrine carbonates. Geological Society of America Special Paper*, 416, 53–74.

Théveniaut, H., Besse, J., Edel, J.B., Westphal, M. and Duringer, P. 1992. A Middle-Triassic paleomagnetic pole for the Eurasian plate from Heming (France). *Geophysical Research Letters*, **19**, 777-780.

Vollmer, F.W. 1995. C program for automatic contouring of spherical orientation data using a modified Kamb method. *Computers and Geosciences*, 21, 31-49.

Vollmer, T., Werner, R., Weber, M., Tougiannidis, N., Röhling, H.G. and Hambach, U. 2008. Orbital control on Upper Triassic Playa cycles of the Steinmergel-Keuper (Norian): A new concept for ancient playa cycles. *Palaeogeography, Palaeoclimatology, Palaeoecology*, 267, 1-16.

Walderhaug, H. 1993. Rock magnetic and magnetic fabric variations across three thin alkaline dykes from Sunnhordland, western Norway; influence of initial mineralogy and secondary chemical alterations. *Geophysical Journal International*, 115, 97-108.

Whiteside, J.H., Olsen P.E., Eglinton, T., Brookfield M.E. and Sambrotto R.N. 2010. Compound-specific carbon isotopes from Earth's largest flood basalt eruptions directly linked to the end-Triassic mass extinction. *Proc. Nation. Acad. Sci*., 107**,** 6721–6725.

Zeigler, K.E., Parker, W.G. and Martz, J.W. 2017. The lower Chinle Formation (Late Triassic) at Petrified Forest National Park, southwestern USA: A case study in magnetostratigraphic correlations. *In:* Ziegler, K.E and Parker, W.G. (eds). *Terrestrial depositional systems*, 237-277, Elsevier. doi.org/10.1016/B978-0-12-803243-5.00006-6

Ziegler, K.E. and Geissman, J.W. 2011. Magnetostratigraphy of the Upper Triassic Chinle Group of New Mexico: Implications for regional and global correlations among Upper Triassic sequences. *Geosphere,* 7, 802-829.